COMPARISON OF NUMERICAL MODELS AND APPLICATION TO TROPICAL CYCLONE DORIAN

A THESIS SUBMITTED TO
THE GRADUATE SCHOOL OF NATURAL AND APPLIED SCIENCES
OF
MIDDLE EAST TECHNICAL UNIVERSITY

BY

GÖKÇE ÖMEROĞLU

IN PARTIAL FULFILLMENT OF THE REQUIREMENTS
FOR
THE DEGREE OF MASTER OF SCIENCE
IN
CIVIL ENGINEERING

JUNE 2021

Approval of the thesis:

COMPARISON OF NUMERICAL MODELS AND APPLICATION TO TROPICAL CYCLONE DORIAN

submitted by **GÖKÇE ÖMEROĞLU** in partial fulfillment of the requirements for the degree of **Master of Science** i**n Civil Engineering, Middle East Technical University** by,

Prof. Dr. Halil Kalıpçılar
Dean, Graduate School of **Natural and Applied Sciences** _____

Prof. Dr. Ahmet Türer
Head of the Department, **Civil Engineering** _____

Prof. Dr. Ahmet Cevdet Yalçıner
Supervisor, **Civil Engineering, METU** _____

Examining Committee Members:

Assist. Prof. Dr. Cüneyt Baykal
Civil Engineering Dept, METU _____

Prof. Dr. Ahmet Cevdet Yalçıner
Civil Engineering Dept, METU _____

Assoc. Prof. Dr. Utku Kanoğlu
Department of Engineering Sciences., METU _____

Assist. Prof. Dr. Gülizar Özyurt Tarakcıoğlu
Civil Engineering Dept., METU. _____

Assist. Prof. Dr. Doğan Kısacık
Civil Engineering Dept., İzmir Institure of Technology _____

Date: 30.06.2021

I hereby declare that all information in this document has been obtained and presented in accordance with academic rules and ethical conduct. I also declare that, as required by these rules and conduct, I have fully cited and referenced all material and results that are not original to this work.

Name Last name : Gökçe Ömeroğlu

Signature :

ABSTRACT

COMPARISON OF NUMERICAL MODELS AND APPLICATION TO TROPICAL CYCLONE DORIAN

Ömeroğlu, Gökçe
Master of Science, Civil Engineering
Supervisor : Prof. Dr. Ahmet Cevdet Yalçıner

June 2021, 85 pages

Coasts are important areas where the vast majority of the world's population lives, have important natural resources and ecosystems, and provide socio-economic opportunities for societies. However, coastal areas are under threat due to different natural disasters such as storms, tsunamis and floods that cause loss of life and property. With the rapid development of hardware and software technologies, many programs that play an important role in the assessment of the natural disasters have achieved to perform high level numerical modeling. In this thesis, Benchmark Problems of the National Tsunami Hazard Mitigation Problems (Benchmark Problem 2, Tohoku tsunami in Hilo harbor Hawaii and Benchmark Problem 4, Seaside Oregon State University Experiments) are simulated with NAMI DANCE and DELFT3D numerical models. The results of the models are compared with the field and experimental data. It is seen that the computed results are in fairly well aggrement with the field and experimental data. Furthermore, the tropical cyclone Dorian occurred in the western Atlantic and Caribbean in September 2019 was simulated by the numerical model NAMI DANCE with its new module solving tropical cyclone events. The numerical results have also been compared with the observations and records at different locations in Caribbean and Western Atlantic coasts.

Keywords: Tropical Cyclone, benchmark, tsunami, numerical modeling, Dorian

ÖZ

SAYISAL MODELLERİN KARŞILAŞTIRILMASI VE TROPİKAL SİKLON DORİAN UYGULAMASI

Ömeroğlu, Gökçe
Yüksek Lisans, İnşaat Mühendisliği
Tez Yöneticisi: Prof. Dr. Ahmet Cevdet Yalçıner

Haziran 2021, 85 sayfa

Kıyılar, dünya nüfusunun büyük çoğunluğunun yaşadığı, önemli doğal kaynaklara ve ekosistemlere sahip, toplumlar için sosyo-ekonomik fırsatlar sunan önemli alanlardır. Ancak kıyı alanları, can ve mal kaybına neden olan fırtına, tsunami ve sel gibi birçok doğal afetler nedeniyle tehdit altındadır. Donanım ve yazılım teknolojilerinin hızla gelişmesiyle birlikte doğal afetlerin değerlendirilmesinde de önemli rol oynayan birçok program üst düzey sayısal modelleme yapmayı başarmıştır. Bu tezde, Ulusal Tsunami Tehlike Azaltma Problemlerinin iki farklı Kıstas Problemi (Kıstas Problemi 2, Hilo Harbor Hawaii'deki Tohoku tsunami ve Kıstas Problemi 4, Seaside Oregon Eyalet Üniversitesi Deneyleri) NAMI DANCE ve DELFT3D sayısal modelleri ile benzetilmiş, modellerin sonuçları saha ve deneysel verilerle karşılaştırılmıştır. Hesaplanan sonuçların saha ve deneysel verilerle iyi bir uyum içinde olduğu görülmektedir. Ayrıca Eylül 2019'da Batı Atlantik ve Karayipler'de meydana gelen tropikal siklon Dorian, tropikal siklon olaylarını çözen yeni modülü ile NAMI DANCE sayısal modeli ile benzetimi yapılmıştır. Sayısal sonuçlar da Karipler ve Batı Atlantik kıyılarında farklı yerlerdeki gözlem ve kayıtlarla karşılaştırılmıştır.

Anahtar Kelimeler: Tropik Fırtınalar, kıstas problemleri, tsunami, sayısal modelleme, Dorian

I dedicate this thesis to my beloved family and my niece Elif Deniz.

ACKNOWLEDGMENTS

First of all, I would like to state my deepest gratitude to my supervisor Prof. Dr. Ahmet Cevdet Yalçıner, for his endless support and supervision with his valuable knowledge and experience. I am so grateful for his contribution and patience to me both in my educational, social, and business life.

I would like to thank Prof. Dr. Ayşen Ergin for her understanding, love, and contribution to my education. I met and loved Coastal Engineering for the first time with her course and decided to continue with this field.

I also would like to thank Assist. Prof. Dr. Gülizar Özyurt Tarakcıoğlu for her contribution to my education, support, and suggestions on my Coastal Engineering path.

I am very grateful to Assist. Prof. Dr. Cüneyt Baykal for his improvement on my Coastal and Ocean Engineering education with his very valuable knowledge.

Also, I am very gratefully thankful to Dr. Işıkhan Güler for his supports and contributions.

I would like to thank Ph.D. candidate Gözde Güney Doğan for her valuable contributions and support to my study. I also extend my thanks to my Coastal Engineering family.

My deepest thanks are also extended to my dear family. They always believed in me and encouraged me. I am very thankful to them for their endless support, endless love, and patience in my all life. I also would like to thank my friends who always give me motivation and encouragement.

Finally, I would like to express my grateful thanks to Mustafa Kemal Atatürk for establishing this free country that we will research, study and develop. I will always follow his path and directions.

TABLE OF CONTENTS

LIST OF TABLES

TABLES

LIST OF FIGURES

FIGURES

CHAPTER 1

INTRODUCTION

Coastal areas are significant geographic areas with substantial natural resource potential and biodiversity, contributing important economic facilities for society. In the Ocean Conference 2020 of the United Nations, it is stated that about 680 million of the population live around low-altitude coastal regions, which is predicted to rise to a billion by 2050. On the other hand, coastal regions are dynamic systems and pose a significant threat to human habitation because they are vulnerable to water-related challenges like storms, floods, and tsunamis, some of the most catastrophic natural hazards associated with these dynamics.

Tsunamis are the damaging long-period waves created by different causes. These sources are often below the sea surface, for instance, seismic movements, submarine landslides, or volcanic eruptions; however, there are also sources above the sea surface, such as meteorological events or asteroid cases (DOGAN, G. G. et al., 2021). The main properties of tsunami are represented in Figure 1.1.

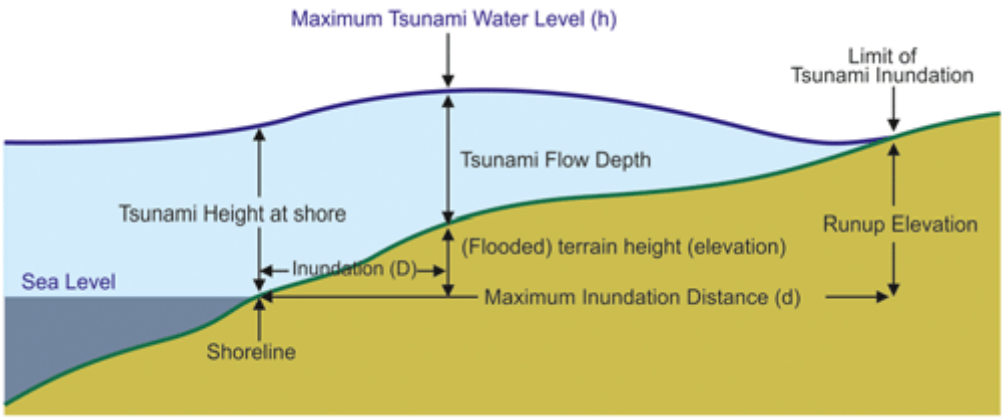

Figure 1.1 The anatomy of tsunami (Lekkas, E. L. et al., 2013)

According to National Hurricane Center, a tropical cyclone is a common term for a low-pressure system rotating around its center and move in an orbit over the tropical area. Tropical cyclones receive their energy from the differences between vertical temperatures having a warm core. In the Northern Hemisphere, tropical cyclones rotate counterclockwise motion. They are classified as in Table 1.1 regarding Saffir-Simpson Hurricane wind scale (NOAA's Atlantic Oceanographic and Meteorological Laboratory, 2021).

Table 1.1 Classification of tropical cyclone

Class	**Wind (km/h)**
Tropical Depression	< 64
Tropical Storm	64-117
Hurricane Category 1	118-152
Hurricane Category 2	153-176
Hurricane Category 3	177-207
Hurricane Category 4	208-250
Hurricane Category 5	>251

The tracks and intensity of tropical storms overworld are shown in Figure 1.2 (NASA Earth Observatory).

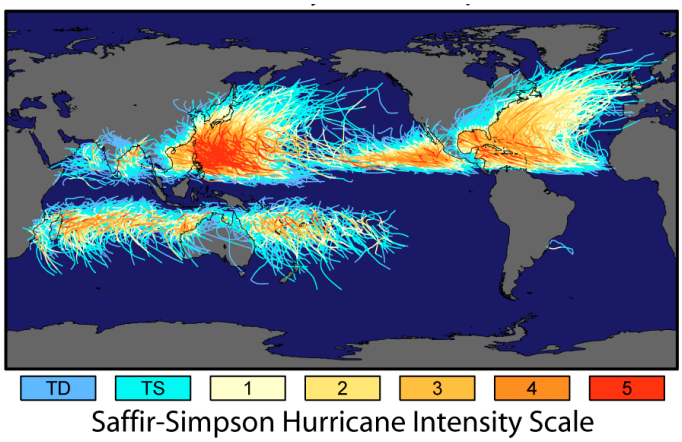

Figure 1.2 The tracks and intensity of tropical storms overworld Credit by Robert A. Rohde (Source: earthobservatory.nasa.gov)

As a result of the accelerated development of computer technologies, many numerical modeling programs have been developed and have become applicable to coastal seas' hydrodynamic problems. Numerical modeling is an important tool for natural disaster simulations. Measures can be taken to predict where and to what extent the damages may occur, and the precautions can be taken to reduce the damages. Especially as a result of global warming, the increase in the seas' temperature will create more low pressure and cause the tropical storms to increase even more, which is already happening too much and causing damage. Therefore, modeling plays a significant role in hazard assessment.

In this thesis, benchmarking problems are conducted with NAMI DANCE and DELFT3D models. Benchmark Problem 2 and Benchmark Problem 4 of the National Tsunami Hazard Mitigation Problem are simulated to validate the models. The results were compared with the measured data and each other. It is seen that models have a similar trend generally. Also, the Dorian tropical cyclone in the western Atlantic in 2019 was simulated with the latest module of NAMI DANCE solving storm surge cases.

Chapter 2 presents a brief literature survey on numerical modeling and applications with NAMI DANCE and DELFT3D. Recent studies on numerical modeling with NAMI DANCE and DELFT3D are summarized.

In chapter 3, NAMI DANCE and DELFT3D are introduced, and the theoretical frameworks of models are explained briefly.

Chapter 4 includes benchmark problems which are 11 March 2011 Japan Tsunami waves at Hilo Harbor, Hawaii and Seaside Oregon State University Model Lab. Benchmarking are proceed with NAMI DANCE and DELFT3D models. Regarding the time series of water surface elevations and current velocities, the results of the simulations are provided by presenting graphical comparisons with the measured data. In addition, tropical cyclone Dorian is studied as a case study by using NAMI DANCE in Chapter 5.

Finally, Chapter 6 summarizes the study with comprehensive numerical model comparisons and future recommendations.

CHAPTER 2

LITERATURE REVIEW

There are many studies tropical cyclone on numerical modeling applications using different methods and processing techniques. Likewise, storm surge and also tsunami numerical models are also studied. Since it would not be possible to summarize all of these studies in this thesis, the most recently studied applications are summarized in chapter 2.1.

2.1 Numerical Modeling Overview

There are a variety of coastal models and modeling approaches that address to solve the coastal water process and coastal problems. It is possible to base the numerical method on the finite difference method, finite element method, finite volume method, boundary element method, or Eulerian-Lagrangian method. There are different options of performing such a method: implicit, semi-implicit, characteristic-based, or explicit. The function's form is of the lowest, second or higher order. The model can be simplified into various spatial scales, i.e., a 1D model, a 2D depth-integrated model, a 2D lateral-integrated model, 2D layered model, and a 3D model (Chau, 2010).

Tsunami models are based on different governing equations, numerical methods, spatial and temporal discretization procedures, and wetting-drying methods.

Based upon finite difference methodology, in the 1990s, the tsunami propagation model known as TUNAMI (Goto et al., 1997) was developed based on nonlinear shallow water equations. For this model, the kinematics of surface elevation along the shoreline is calculated by parameterizing a water flux amount, the "discharge"

(Imamura, 1996). In a conservative flux-conserving manner, nonlinear shallow water equations are constructed.

Another numerical model MOST, often widely used in the operational tsunami models, is separating tsunami, which computes tsunami propagation using a variable space grid or free variables to imitate theoretical dispersion and enabling extension to simulate loosely dispersive tsunamis (Titov and Synolakis, 1995).

GeoClaw is yet another tsunami simulation model. It uses the nonlinear shallow water equations to measure the transition of fluid kinematics throughout nested grids. To manage this, GeoClaw uses a standard mesh scheme with an infinite number of nested layers. As the measurement proceeds, individual grid cells are classified for refinement, using a parameter such as a wave height or defining the area of concern. The disturbed water fragments or those in defined regions are routinely better resolved (Berger and Leveque, 1998).

Another model, FUNWAVE, was developed by Kirby et al. (1998) based on fully nonlinear Boussinesq equations of Wei et al. (1995). In 2012, Shi et al. developed the version of the Total Variation Diminishing of FUNWAVE. FUNWAVE-TVD

Numerical model contains all the essential features required for tsunami forecasting, like bottom friction, runup, dissipation of energy, and a turbulence model (Shi et al., 2012).

Various numerical models were applied and tested during a workshop of National Tsunami Hazard Mitigation Program (NTHMP) conducted in 2011 at Texas A&M University. This assessment focused on the current standard, which offers a set of benchmark problems for tsunami models to simulate tsunami processes accurately. Table 2.1 shows the general characteristics of the tsunami numerical models chosen for comparisons (Horrillo et al., 2014). Two more workshops of NTHMP program have also been organized in 2015 (Lynett et al., 2017) and in 2017 http://www1.udel.edu/kirby/landslide. Tsunami numerical models used in 2015 NTHMP Portland workshop are given in Lynett et al. (2017). Table 2.2 shows the

summary of tsunami numerical models for the benchmark tests of 2015 NTHMP Portland workshop (Lynett et al., 2017).

Table 2.1 Summary of Tsunami models' characteristics chosen for comparison in NTHMP 2011 workshop (Horrillo et al., 2014)

Model/features	ALASKA	ATFM	BOSZ	FUNWAVE	GeoClaw	MOST	NEOWAVE	SELFE	THETIS	TSUNAMI3D
Approximation	NSWE	Hyd/non-hyd	FNBM	FNBM	NSWE	NSWE	Hyd/non-hyd	Hyd/non-hyd	3-D NS	3-D NS
Wave dispersion	No	Yes (optional)	Yes	Yes	No	No	Yes	Yes (optional)	Yes	Yes (optional)
Grid nesting	Two-way	Two-way (submeshes)	No	One-way	Two-way (Adaptive mesh refinement)	One-way	Two-way	Two-way unstructured mesh	Structured variable mesh	Structured variable mesh
Coordinate system	Cartesian/ spherical	Cartesian/ spherical	Cartesian	Cartesian/ spherical	Cartesian/ spherical	Cartesian/ spherical	Cartesian/ spherical	Cartesian/ spherical	Cartesian/ cylindrical	Cartesian
Numerical scheme	Finite difference	Finite difference	Finite volume	Finite difference/ finite volume	Finite volume	Finite difference	Finite difference	Finite element/ finite volume	Finite volume	Finite volume
Tsunami source	Coseismic ? landslide	Coseismic	Coseismic	Coseismic ? landslide (initializ. THETIS)	Coseismic ? landslide	Coseismic	Coseismic ? landslide (initializ. TSUNAMI3D)	Coseismic	Landslide (coupled to FUNWAVE)	Landslide (coupled to NEOWAVE)
Run-up approach	Moving boundary	Volume of fluid	Shock-capturing/ Riemann solution	Slot technique	Shock-capturing/ Riemann solution	Horizontal projection	Horizontal projection	Iterative projection	Volume of fluid	Volume of fluid
Parallelization	MPI	Co-array	OpenMP	MPI	OpenMP	OpenMP	No	MPI	MPI	OpenMP/MPI
Documentation	Limited	Limited	Limited	Yes	Yes	Limited	Yes	Yes	Yes	Limited
Execution	Graphics interface	Command line	Command line/ graphics interface	Command line	Command line	Graphics interface	Command line	Command line	Command line	Command line

Table 2.2 Summary of Tsunami numerical models for comparison in NTHMP 2015 workshop (Lynett et al., 2017)

Model #	Model name	Equations solved [spatial dimensions]	Class	Numerical approach	Numerical treatment of convection terms	Numerical accuracy of other gradient terms	Numerical treatment of time integration
1	ALASKA GI'-T	Nonlinear shallow water [2D]	I	FD	Upwind (1st-order accurate)	Centered (2nd-order accurate)	Semi-implicit (1st-order accurate)
2	NAMI DANCE	Nonlinear shallow water [2D]	I	FD	Upwind (1st-order accurate)	Centered (2nd-order accurate)	Explicit (2nd-order accurate)
3	MOST	Nonlinear shallow water [2D]	I	FD	Centered (2nd-order accurate)	Centered (2nd-order accurate)	Explicit (1st-order accurate)
4	Cliffs	Nonlinear shallow water [2D]	I	FD	Centered (2nd-order accurate)	Centered (2nd-order accurate)	Explicit (1st-order accurate)
5	GeoClaw	Nonlinear shallow water [2D]	I	FV	Limiter-based (1st-order near shocks, 2nd-order when smooth)	Centered (2nd-order accurate)	Explicit (2nd-order accurate)
6	GeoClaw –AECOM	Nonlinear shallow water [2D]	I	FV	Limiter-based (1st-order near shocks, 2nd-order when smooth)	Centered (2nd-order accurate)	Explicit (2nd-order accurate)
7	Tsunami-HySEA	Nonlinear shallow water [2D]	I	FV	Limiter-based (2nd-order near shocks, 3rd-order when smooth)	Centered (2nd-order accurate)	Explicit (3rd-order accurate)
8	pCOULWAVE	Highly nonlinear Boussinesq-type [2D]	II	FV	Limiter-based (2nd-order near shocks, 4th-order when smooth)	Centered (4th-order accurate)	Semi-implicit (4th-order accurate)
9	FUNWAVE-TVD	Highly nonlinear Boussinesq-type [2D]	II	FV/FD	Limiter-based (2nd-order near shocks, 5th-order when smooth)	Centered (4th-order accurate)	Explicit (3rd-order accurate)
10	BOSZ	Weakly nonlinear Boussinesq-type [2D]	II	FV/FD	Limiter-based (2nd-order near shocks, 5th-order when smooth)	Centered (2nd-order accurate)	Explicit (4th-order accurate)
11	NEOWAVE	One-layer, non-hydrostatic [2D]	III	FD	Upwind (1st-order near shocks, 2nd-order when smooth)	Centered (2nd-order accurate)	Semi-implicit (2nd-order accurate)
12	TSUNAMI3D	Navier–Stokes [3D]	III	FD	Upwind (1st-order accurate)	Centered (2nd-order accurate)	Explicit (2nd-order accurate)
13	SCHISM	Navier–Stokes, hydrostatic [3D]	III	FE/FV	Limiter-based (1st-order near shocks, 2nd-order when smooth)	Centered (2nd-order accurate)	Semi-implicit (2nd-order accurate)

Note that in the "Numerical Approach" column, FD = Finite difference, FV = Finite volume, FE = Finite element.

Meteorological parameters form triggering coastal disasters are often cited as one of the significant triggers of coastal disasters. A storm surge happens as an extensive low pressure passes to the coast. While only limited in magnitude, even small atmospheric pressures may produce ocean waves and can result in coastal hazards while dealing with non-uniform bottom topographies or coastal forms. These waves are known as meteorological tsunamis, as the same phenomenon can cause them as tsunami. These waves will cause disruptive events, but the wave's cumulative impact would be minimal relative to the seismic tsunami (Choi and Jo, 2018).

Before the computer age, storm surge predictions were studied using analytical, empirical, graphical, and statistical techniques. However, nowadays, numerical methods are used almost completely. Until the late 1970s, square or rectangular grid finite-difference models were typically used to increase resolution close to the shorelines. However, this approach was not coherent with the irregular nature of coastlines. Since the late 1970s, finite element models of irregular triangular grids have been developed to prevent these issues and improve the resolution of the coastal geometry and shallow water topography (Horsburgh and De Vries, 2011).

The Hurricane Weather Research and Forecast (HWRF), developed by the National Centers for Environmental Prediction of NOAA, is a high-resolution atmosphere-ocean coupled modeling system used to predict the intensity and track of tropical cyclones (Mohanty, 2016). The storm-centered operating HWRF has utilized the Message Passing Interface Princeton Ocean Model for Tropical Cyclones (MPIPOM-TC) as an oceanic component. The Princeton Ocean Model is the inspiration for the MPIPOM-TC oceanic model (Blumberg and Mellor, 1987). Utilizing input and output concerning the netCDF file, the MPIPOM-TC is computer-efficient and scalable. MPIPOM-TC also helps to initialize a range of global ocean components (Yablonsky et al., 2015).

Alaka et al. (2020) have studied the advanced multiple storms atmosphere-ocean connectivity system, which has been developed and evaluated in the Basin Scale Hurricane Weather Research and Forecasting (HWRF-B) Model that is a version of HWRF. HWRF-B can design several storm-subsequent nested fields to generate high-resolution forecasts for many tropical cycles in the same prediction. The reliability of HWRF-B was assessed and compared to the satellite data with the simulated track, structure (surface wind radii, for instance), intensity, and intensity change by focusing on five case studies, namely; Tropical Storm Mario, Hurricane Florance, Hurricane Dorian, Hurricane Irma, and Hurricane Kiko. For five case studies, the sea-surface temperatures dropped by 1-8 ° C demonstrate the usefulness of the model for analyzing the effect of the ocean over the tropical cyclone intensity prediction. Such findings indicate the significance of a modeling system with many storms and rely on the proper implementation of the multiple storms connecting system. Future tropical cyclone models of NOAA would profit from a multi-storm copulating system, whose efficiency and performance are shown in the study in the HWRF B. (Alaka et al., 2020)

The analysis of weather like forecasting, monitoring, and warning includes various data sources and instruments, such as satellite imaging and derivative products. When the in-site observations are missing or are not easily accessible, satellite data offers information. Passive microwave satellite data are often used to facilitate weather analysis and forecasting. Jelenak et al. (2020) compare NOAA the Advanced Scanning Radiometer hurricane Dorian observations –2 (AMSR-2) EDR results with storm finding in the National Hurricane Center - Hurricane Dorian results. NOAA AMSR-2, which is part of a product set of the National Weather Service forecast, is utilized in daily operational activities on a routine basis. While the output of Microwave Imagery is primarily utilized for hurricane forecast, Jelenak et al. (2020) investigate the effectiveness of other ocean data in analyzing the development of Hurricane Dorian from 24 August to 6 September.

After the underprediction of the intensity formation of Tropical Cyclone Dorian in Tropical Cyclone forecast models, Aristizabal-Vargas et al. (2020) are reported that an accurate description of the ocean-upper elements that drive air-ocean heat fluxes in combined atmosphere-ocean models is required to get a precise storm intensity prediction. Aristizabal-Vargas et al. (2020) evaluate a few sea surface measurements relating to air-sea heat fluxes in one of the Tropical Cyclone forecasting models of NOAA: HWRF2019-POM, which is denoted from climate science, as well as two experimental models: HWRF2020-HYCOM and HWRF2020-POM, configured from the Real-Time Ocean Forecasting System. The findings are compared to predictions from the Global Ocean Forecasting System, a data assimilation model. It is observed that, although all of the models have a high capability in forecasting temperature and concentration throughout the whole water column, the model's performance deteriorates significantly for the ocean surface measurements considered. Furthermore, among the three models, HWRF2020-HYCOM has the highest performance for sea surface measurements. (Aristizabal-Vargas et al., 2020)

CHAPTER 3

THEORETICAL FRAMEWORK

The shallow water equations explain a small layer of constant density fluid that is in hydrostatic equilibrium. They are applicable when the horizontal flow scale is significantly greater than the vertical flow. The shallow-water equations may correctly predict the tsunami's propagation as it has a long wavelength and period.

The nonlinear convective components are excluded from the linear shallow water equations that are the primary type of equations utilized in the motion of tsunami wave prediction. Numerical models based on the linear theory are favored for predicting tsunami wave propagation over the deep sea because they need a comparatively modest amount of computing. However, the linear long-wave concept is no longer valid due to nonlinear circumstances in shallower areas since nonlinear effects become more significant when tsunami waves reach shallower zones. Despite the challenges, nonlinear shallow water equations that incorporate the impact of bottom friction upon tsunami wave motion explain tsunami behavior in shallow water zones.

3.1 NAMI DANCE Numerical Model Background

Profs. Andrey Zaytsev, Ahmet Yalciner, Anton Chernov, Efim Pelinovsky, and Andrey Kurkin created NAMI DANCE specifically for tsunami simulation. It offers tsunami production, propagation, and inundation processes, computational simulations, and convenient presentation. It is coded in the C++ programming language and employs the same leap-frog technique numeric solution method as TUNAMI-N2 (Imamura, 1989; Shuto, Goto, and Imamura, 1990). All tsunami parameters can be computed using NAMI DANCE. Also, it animates the propagation of tsunami from source to destination, including inundation, and

offers 3D graphs of sea state at chosen time intervals from various camera locations.

The flow in vertical scale has no impact on the distribution of pressure in the long waves theory. The conservation of mass and momentum in a three-dimensional case is represented by the following system of equations relying on this approach and ignoring vertical acceleration:

$$\frac{\partial \eta}{\partial t} + \frac{\partial u}{\partial x} + \frac{\partial v}{\partial y} + \frac{\partial w}{\partial z} = 0 \quad [3.1]$$

$$\frac{\partial u}{\partial t} + u\frac{\partial u}{\partial x} + v\frac{\partial u}{\partial y} + w\frac{\partial u}{\partial z} + \frac{1}{\rho}\frac{\partial P}{\partial x} + \frac{1}{\rho}\left(\frac{\partial \tau_{xx}}{\partial x} + \frac{\partial \tau_{xy}}{\partial y} + \frac{\partial \tau_{xz}}{\partial z}\right) = 0 \quad [3.2]$$

$$\frac{\partial v}{\partial t} + u\frac{\partial v}{\partial x} + v\frac{\partial v}{\partial y} + w\frac{\partial v}{\partial z} + \frac{1}{\rho}\frac{\partial P}{\partial y} + \frac{1}{\rho}\left(\frac{\partial \tau_{xy}}{\partial x} + \frac{\partial \tau_{yy}}{\partial y} + \frac{\partial \tau_{yz}}{\partial z}\right) = 0 \quad [3.3]$$

$$g + \frac{1}{\rho}\frac{\partial \rho}{\partial z} = 0 \quad [3.4]$$

where z is the Cartesian vertical axis, η is the displacement vertically of the sea surface above the still sea state, ρ is the density of the fluid, P is the pressure, u, v, and w are the velocities of water particles in the x, y, and z directions, and τ_{ij} is the normal or tangential shear stress in the i direction on the j normal plane. (Yalciner et al., 2015)

The hydrostatic pressure $p=\rho g(\eta-z)$ is obtained by combining the momentum equation in the vertical direction and the dynamic state at a surface. The governing equations and boundary conditions may then be used to solve wave propagation issues. The following are the kinetic and dynamic conditions at the surface and bottom:

$$p=0 \text{ at } z=\eta \quad [3.5]$$

$$w = \frac{\partial \eta}{\partial t} + u\frac{\partial \eta}{\partial x} + v\frac{\partial \eta}{\partial y} \text{ at } z=\eta \quad [3.6]$$

$$w = -u\frac{\partial h}{\partial x} - v\frac{\partial h}{\partial y} \text{ at } z=-h \quad [3.7]$$

Where h is the water depth.

The two-dimensional depth-averaged nonlinear shallow water equations using the discharge fluxes are achieved by merging Equations [3.1]– [3.4] from the sea bottom, -h, to the free surface, using the Leibniz integral rule and adding boundary conditions at the seabed and the free surface (Imamura et al., 2006):

$$\frac{\partial \eta}{\partial t} + \frac{\partial M}{\partial x} + \frac{\partial N}{\partial y} = 0 \quad [3.8]$$

$$\frac{\partial M}{\partial t} + \frac{\partial}{\partial x}\left(\frac{M^2}{D}\right) + \frac{\partial}{\partial y}\left(\frac{MN}{D}\right) + gD\frac{\partial \eta}{\partial x} + \frac{\tau_x}{\rho} = A\left(\frac{\partial^2 M}{\partial x^2} + \frac{\partial^2 M}{\partial y^2}\right) \quad [3.9]$$

$$\frac{\partial N}{\partial t} + \frac{\partial}{\partial x}\left(\frac{MN}{D}\right) + \frac{\partial}{\partial y}\left(\frac{M^2}{D}\right) + gD\frac{\partial \eta}{\partial y} + \frac{\tau_y}{\rho} = A\left(\frac{\partial^2 N}{\partial x^2} + \frac{\partial^2 N}{\partial y^2}\right) \quad [3.10]$$

Where; A is the horizontal eddy viscosity considered constant, D is the total water depth, τ_x and τ_y are the bottom frictions in the x and y directions, and finally, the discharge fluxes in the x and y axes are M and N, respectively.

The M and N discharge fluxes are described as follows:

$$M = uD \quad [3.11]$$

$$N = vD \quad [3.12]$$

The friction of bottom is usually represented in the following way:

$$\frac{\tau_x}{\rho} = \frac{1}{2g}\frac{f}{D^2}M\sqrt{M^2 + N^2} \quad [3.13]$$

$$\frac{\tau_y}{\rho} = \frac{1}{2g}\frac{f}{D^2}N\sqrt{M^2 + N^2} \quad [3.14]$$

Where, f is the coefficent of friction. The relation between f and Manning's roughness n is:

$$n = \sqrt{\frac{fD^{1/3}}{2g}} \quad [3.15]$$

Apart from tsunami run-up inland, horizontal eddy turbulence may be ignored compared to bottom friction for tsunami propagation in shallow water. As

a result, the equations following are provided as the model's fundamental equations.

$$\frac{\partial \eta}{\partial t} + \frac{\partial M}{\partial x} + \frac{\partial N}{\partial y} = 0 \quad [3.16]$$

$$\frac{\partial M}{\partial t} + \frac{\partial}{\partial x}\left(\frac{M^2}{D}\right) + \frac{\partial}{\partial y}\left(\frac{MN}{D}\right) + gD\frac{\partial \eta}{\partial x} + \frac{n^2}{D^{1/3}} M\sqrt{M^2 + N^2} = 0 \quad [3.17]$$

$$\frac{\partial N}{\partial t} + \frac{\partial}{\partial x}\left(\frac{MN}{D}\right) + \frac{\partial}{\partial y}\left(\frac{M^2}{D}\right) + gD\frac{\partial \eta}{\partial y} + \frac{n^2}{D^{1/3}} N\sqrt{M^2 + N^2} = 0 \quad [3.18]$$

After that, NAMI DANCE receives the input of the tsunami source and evaluates the propagation, coastal amplification, and inundation on the land using the governing equations succinctly stated above. NAMI DANCE also gives information on the arrival time of the first and maximum waves and the distribution of sea state, flow velocities, and fluxes. Maximum values of water levels, velocities and directions, flow depths, and fluxes calculated during simulation, as well as the Froude Number and time histories of water level variations at chosen gauge points, may well be shown. NAMI DANCE uses the staggered leap-frog method in Finite Difference numerical solution (Yalciner et al., 2015).

3.2 DELFT3D Numerical Model Background

DELFT3D is a 3D modeling package for rivers, estuarine, and coastal areas that investigates hydrodynamics, quality of water, and sediment transport. In the next subsections, the numerical system of DELFT3D is given briefly.

DELFT3D has various modules to solve different problems of coastal and ocean engineering (Figure 3.1, Table 3.1). DELFT3D's FLOW module is a hydrodynamic and sediment transport simulation software in 2D or 3D that estimates non-steady flow and transport event caused by tidal and meteorological forces developed by Delft Hydraulics.

The modules of DELFT3D are given in the following Figure 3.1.

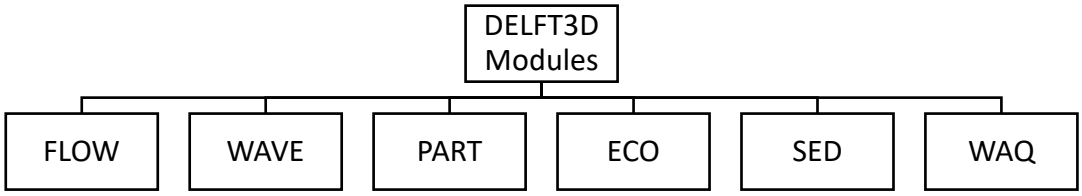

Figure 3.1 DELFT3D Modules

Simulations which can be performed by each module can be stated as in Table 3.1.

Table 3.1 DELFT3D modules capabilities

FLOW	hydrodynamic in 2D or 3D, salinity, temperature, transport, sediment
WAVE	propogation of short waves
PART	tracking of partcile and mid-field water quality
ECO	ecological
SED	transport of cohesive and non-cohesive sediment
WAQ	far-field water quality

The primary goal of the DELFT3D-FLOW numerical model is to solve 1D, 2D, or 3D time-dependent, non-linear differential equations regarding hydrostatic and non-hydrostatic free-surface flow problems on a constructed orthogonal grid to solve problems with complex geometries. On a plane, the equations are written in orthogonal curvilinear coordinates, whereas, on the globe, they are written in spherical coordinates. The equations of conservation of mass, Reynolds averaged Navier-Stokes (RANS), and the transport equations such as sediments, pollutant, salt, and temperature are solved in the DELFT3D-Flow module. Moreover, the changes of the bed level depending on the bottom sediment quantity are computed. DELFT3D-FLOW is available in two modes: hydrostatic and non-hydrostatic. The shallow water equations are governed in hydrostatic modeling, while the Navier-Stokes's equations are considered in non-hydrostatic mode by inserting

non-hydrostatic components into the shallow water equations. To analyze a non-hydrostatic flow case, a fine horizontal grid is required. (Deltares D., 2013)

The 3D governing equations that describe surface-flows may be obtained by averaging across turbulent time scales from the Navier Stokes equations. These equations describe the fundamental principle of the conservation of mass, volume, and momentum.

The three-dimensional hydrostatic shallow water equations are expressed in V-coordinates in vertical and in Cartesian rectangular coordinates in horizontal for the simplicity as follow:

(Hydrostatic flow)

$$\frac{\partial u}{\partial t} + u\frac{\partial u}{\partial x} + v\frac{\partial u}{\partial y} + \frac{\omega}{d+\zeta}\frac{\partial u}{\partial \sigma} - fv = -\frac{1}{\rho}P_u + F_u - \frac{\partial q}{\partial x} + \frac{1}{(d+\zeta)^2}\frac{\partial}{\partial \sigma}\left(v_V \frac{\partial u}{\partial \sigma}\right) \quad [3.19]$$

$$\frac{\partial v}{\partial t} + u\frac{\partial v}{\partial x} + v\frac{\partial v}{\partial y} + \frac{\omega}{d+\zeta}\frac{\partial v}{\partial \sigma} + fu = -\frac{1}{\rho}P_v + F_v - \frac{\partial q}{\partial x} + \frac{1}{(d+\zeta)^2}\frac{\partial}{\partial \sigma}\left(v_V \frac{\partial v}{\partial \sigma}\right) \quad [3.20]$$

$$\frac{\partial \omega}{\partial \sigma} = -\frac{\partial \zeta}{\partial t} - \frac{\partial[(d+\zeta)u]}{\partial x} - \frac{\partial[(d+\zeta)v]}{\partial y} + H(q_{in} - q_{out}) + P - E \quad [3.21]$$

$$\frac{\partial \zeta}{\partial t} + \frac{\partial[(d+\zeta)U]}{\partial x} + \frac{\partial[(d+\zeta)V]}{\partial y} = Q \quad [3.22]$$

$$w = \omega + u\left(\sigma\frac{\partial H}{\partial x} + \frac{\partial \zeta}{\partial x}\right) + v\left(\sigma\frac{\partial H}{\partial y} + \frac{\partial \zeta}{\partial y}\right) + \left(\sigma\frac{\partial H}{\partial t} + \frac{\partial \zeta}{\partial t}\right) \quad [3.23]$$

Where;

u, v, and w	the velocity components in horizontal x,y and in vertical z directions, respectively
ω	the velocity component in the vertical σ-direction
ζ	the water level above defined plane
d	the depth below defined plane
$H=d+\zeta$	the total water depth
t	time
f	Coriolis parameter
g	gravitational acceleration
v_V	the coefficient of the vertical eddy viscosity
q_{in}	the local sources per unit volume
q_{out}	the sinks per unit volume
P	precipitation
E	evaporation

In the last decades, there has been broad use of 3D hydrostatic models of shallow water to comprehend and evaluate free surface flow. In most instances, the flows are of the kind of boundary layer, such that the vertical acceleration part is relatively low. In this context, the vertical pressure distribution is considered hydrostatic, ignoring the pressure's hydrodynamic component. This results in the shallow water equations presented in the last section. The vertical acceleration can not be ignored. The non-hydrostatic pressure component is essential to many small-scale fluxes, such as over-altering bottom topography, orbital movements in short-wave or intense vertical circulations. Shallow-water flow requirements have been eliminated, and the hydrodynamic pressure component must be addressed to get physically realistic flow behavior. This non-hydrostatic model is included in DELFT3D-FLOW as follow:

(Nonhydrostatic flow)

$$\frac{\partial u}{\partial t} + u\frac{\partial u}{\partial x} + v\frac{\partial u}{\partial y} + w\frac{\partial u}{\partial z} - fv = -\frac{1}{\rho}P_u + F_u - \frac{\partial q}{\partial x} + \frac{1}{(d+\zeta)^2}\frac{\partial}{\partial z}\left(v_v\frac{\partial u}{\partial z}\right) \quad [3.24]$$

$$\frac{\partial v}{\partial t} + u\frac{\partial v}{\partial x} + v\frac{\partial v}{\partial y} + w\frac{\partial v}{\partial z} - fu = -\frac{1}{\rho}P_v + F_v - \frac{\partial q}{\partial y} + \frac{1}{(d+\zeta)^2}\frac{\partial}{\partial z}\left(v_v\frac{\partial u}{\partial z}\right) \quad [3.25]$$

$$\frac{\partial w}{\partial t} + u\frac{\partial w}{\partial x} + v\frac{\partial w}{\partial y} + w\frac{\partial w}{\partial z} = -\frac{1}{\rho}P_w + F_w - \frac{\partial q}{\partial x} + \frac{1}{(d+\zeta)^2}\frac{\partial}{\partial z}\left(v_v\frac{\partial w}{\partial z}\right) \quad [3.26]$$

CHAPTER 4

COMPARISON OF MODELS BY BENCMARKING

The two stages of a study that a numerical code should go through when evaluating the quality of a Computational Fluid Dynamics (CFD) model are verification and validation (Maguire, 2011). Validation and verification procedures are critical components in the building of a numerical model. The numerical model is submitted to a set of benchmark tests considered trustworthy by the scientific community to perform the verification and validation procedure. Benchmarking of numerical models is divided into three categories as analytical, experimental, and field benchmarking. (Synolakis et al., 2007)

In the NTHMP tsunami current workshop (http://coastal.usc.edu/currents_workshop/index.html), five benchmark problems are given for validation and comparison of the tsunami numerical models.

In this chapter, benchmark problems which are 11 March 2011 Japan Tsunami waves at Hilo Harbor (BMP 2), Hawaii and Seaside Oregon State University Model Lab. Benchmarking (BMP 4) are proceed with NAMI DANCE and DELFT3D models. The reason why these two problems were selected for tesgitng and comparisons of the models is that one is a field (BMP 2) and the other is an experimental Benchmark Problem (BMP 4).

4.1 Benchmark Problem 2 of NTHMP: 2011 Tōhoku Tsunami in Hilo Harbor, Hawaii

The benchmark problem 2 and the procedure to apply models are described and the computed results are presented, compared and discuss in the following.

4.1.1 Problem Description

On March 11, 2011, at 05:46 UTC, an earthquake struck Japan's north-east coasts with a magnitude of 9.1 (Hayes et al., 2016). This earthquake's epicenter is at the coordinates of 38.297°N 142.373°E, having a focal depth of 29 kilometers (USGS, 2011) (Figure 4.1). This event, called the Great East Japan Earthquake, took fourth place on the list of 20 largest earthquakes in the world of the U.S. Geological Survey.

Figure 4.1 The epicenter of the 11 March 2011 Japan Earthquake (Zhang, 2014)

This earthquake caused one of the mega earthquake-generated tsunamis after the Sumatra and Chile Tsunamis that hit Japan coasts and various Pacific Ocean regions. In the Sendai region, where the maximum inundation height was 19.5 meters, the propagation of tsunami was more than 5 kilometers (Figure 4.2). The narrow bays in this region caused the largest inundation of tsunami waves (Mori et al., 2011). 22,626 people are estimated to have died (Yalciner et al., 2011).

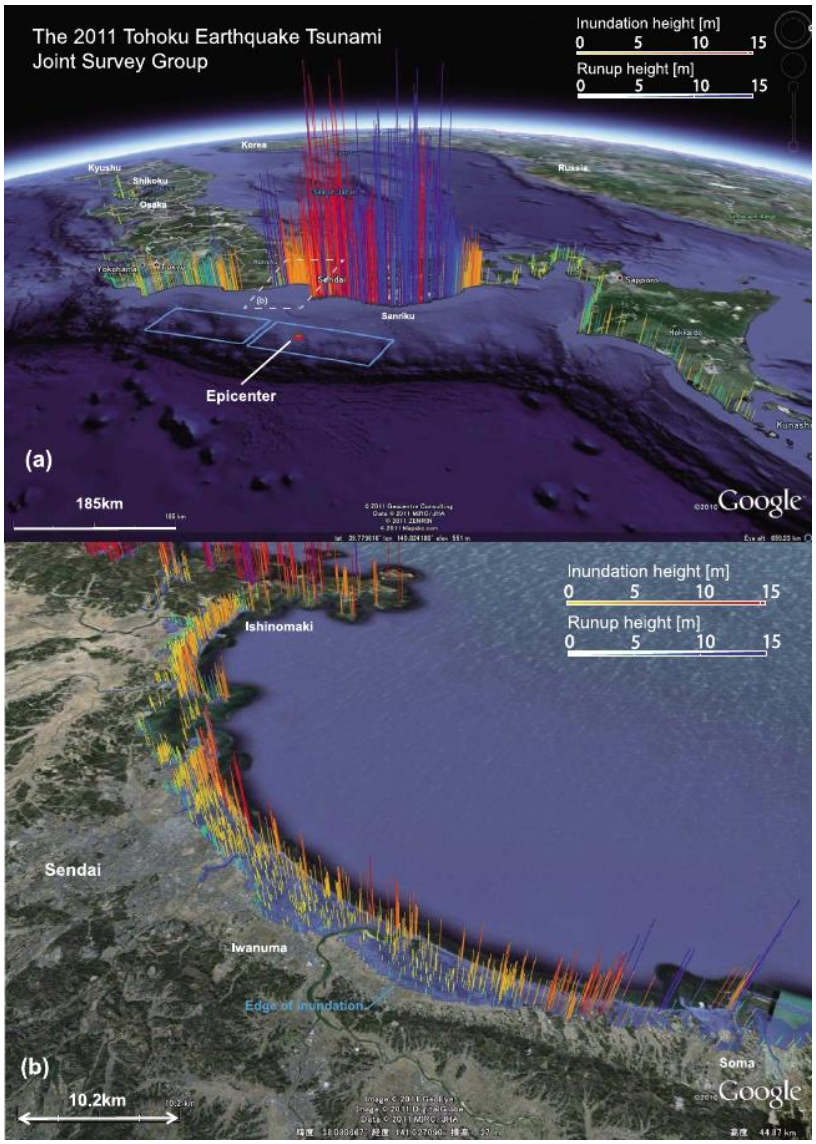

Figure 4.2 Measured inundation (red color bar) and run-up (blue color bar) heights along the east coast of Japan view (a) and Sendai region (b), (Mori et al., 2011)

The Pacific Tsunami Warning Center gave a warning for Hawaii to be taken precautions. The propagation and arrival times of waves in the Pacific Ocean are shown in Figure 4.3 and Figure 4.4, respectively, published by National Tsunami Warning Center, NOAA/NWS. The waves have reached Hawaii after 7 hours of the earthquake (National Tsunami Warning Center, NOAA/NWS, 2011).

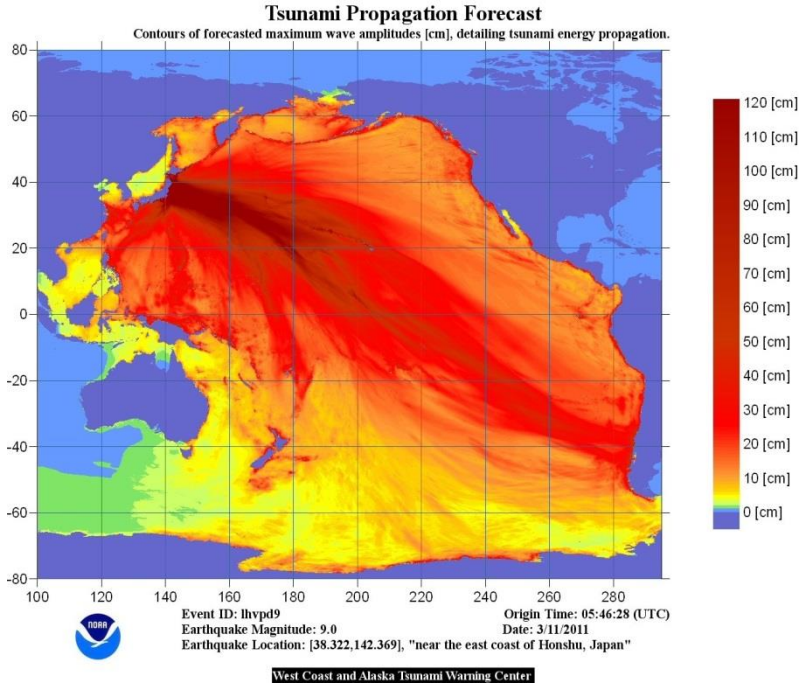

Figure 4.3 The propagation and highest amplitude of tsunami waves (National Tsunami Warning Center, NOAA/NWS, 2011)

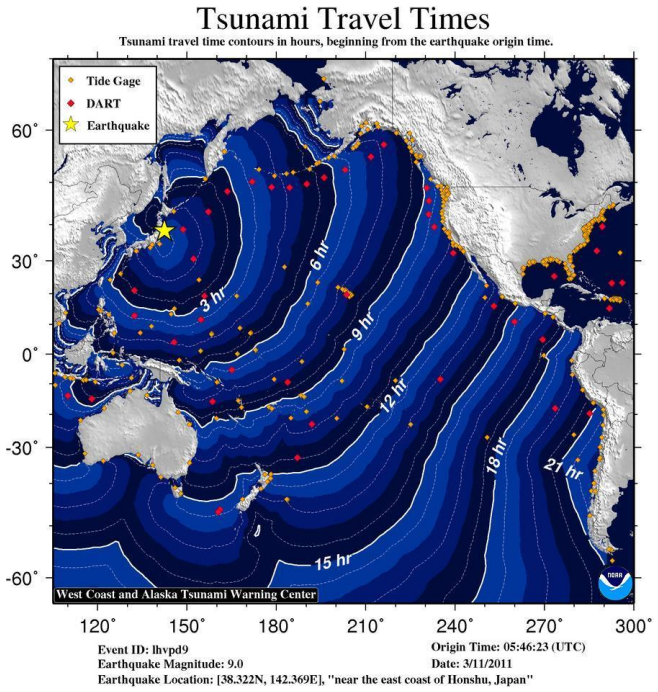

Figure 4.4 The arrival time of tsunami waves in the Pacific Ocean National Tsunami Warning Center, NOAA/NWS, 2011)

In this earthquake-generated tsunami, 328 acoustic doppler current profiler were measured time series of water velocity at varying depths around the Hawaiian Islands, USA, in 18 locations (Arcos and LeVeque, 2014) (Figure 4.5 and Table 4.1).

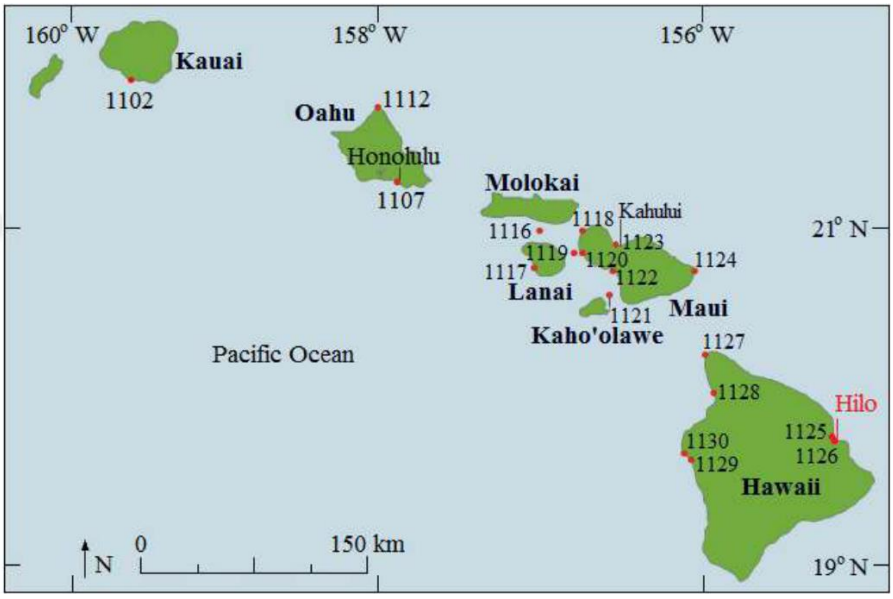

Figure 4.5 Location of ADCPs around Hawaii, USA (Arcos and LeVeque, 2014)

Table 4.1 The descriptions of current meters at stations (Arcos and LeVeque, 2014)

Station id	Station name	Latitude (°)	Longitude (°)	Top sensor depth (m)	Bottom sensor depth (m)	Number of current meters	Depth at station (m)	Maximum observed velocity (m/s)
HAI1102	Port Allen	21.89638	200.40768	2.04	7.04	6	12.56	1.62
HAI1107	Approach to Honolulu harbor	21.29147	202.12623	2.19	12.19	11	14.9	0.39
HAI1112	Kahuku point	21.72998	202.01005	7.65	57.64	26	67.37	0.81
HAI1116	Kalohi channel	21.0033	203.04117	9.36	72.36	22	105.06	Tsunami within background currents
HAI1117	Kaumalapau harbor	20.78462	203.00758	2.77	13.75	12	19.62	Tsunami within background currents
HAI1118	Hawea point	21.00178	203.30818	8.08	74.07	34	83.69	0.51
HAI1119	Auau channel East side	20.86727	203.25283	7.89	63.89	29	73.51	0.43
HAI1120	Lahaina	20.86845	203.31472	1.98	14.97	14	20.48	0.52
HAI1121	Alalakeiki channel	20.61252	203.49188	16.92	124.91	28	153.98	0.76
HAI1122	Maalaea bay	20.76525	203.50765	6.13	40.11	18	49.83	0.41
HAI1123	Kahului harbor	20.90213	203.52825	4.3	11.31	8	14.02	1.84
HAI1124	Hana bay	20.76123	204.0219	3.05	16.06	14	21.19	0.24
HAI1125	Approach to HiloHarbor	19.74517	204.91802	2.59	16.58	15	19.29	0.7
HAI1126	Hilo harbor	19.74167	204.93003	1.74	9.75	9	12.46	1.04
HAI1127	Upolu point	20.26502	204.09843	10.39	62.39	27	72.1	Tsunami within background currents
HAI1128	Kawaihae	20.04108	204.15837	6.04	38.04	17	41.74	0.37
HAI1129	Entrance Kailua Kona	19.6351	204.00085	2.87	18.87	17	20.48	0.35
HAI1130	Honokohau	19.6678	203.9681	6.98	46.97	21	56.6	Tsunami within background currents

Table 4.1 above shows that the observed velocities obtained from current meters are due to the 11 March 2011 Tōhoku Tsunami around Hawaii, USA.

The datasets recorded due to the tsunami have quality measurements and coverage, contributing validation of model and scientific research. Benchmark Problem 2 of NTHMP (National Tsunami Hazard Mitigation Problem) - Mapping and Modeling Benchmarking Workshop introduces a part of this dataset at Hilo Harbor. The location of Hilo from Google Earth is provided for a clear understanding in Figure 4.6.

The breakwater protecting the town of Hilo Bay is shown in Figure 4.7.

BMP 2 (Benchmark Problem 2) has been diminished in order to remove variation in the force of the incident wave. For the bathymetry data, this "reduction" has been applied as a flattening of the grid at 30 meters depth; in the offshore part of the bathymetry, which causes no depths larger than 30 m. The bathymetry data is supplied in (latitude, longitude) on a 1/3 arcsec grid (Figure 4.8).

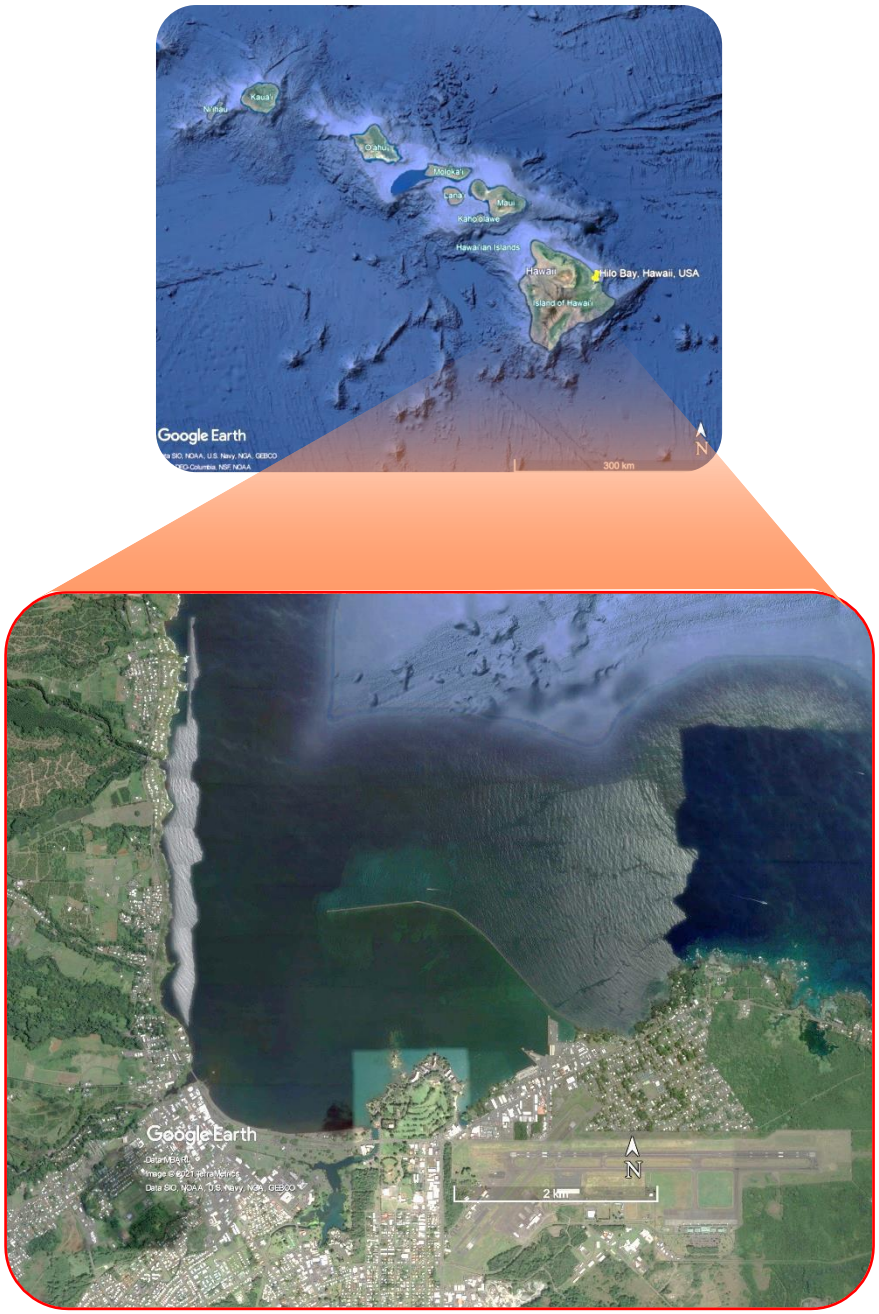

Figure 4.6 Google Earth view of Hawaii Islands and Hilo Harbor

Figure 4.7 Hilo Bay (Credit: Hollyn Johnson for University of Hawaii)

BMP 2 dataset covers the time series of Hilo Tide Station and Acoustic Doppler Current Profiler HA1126. The location of Hilo Tide Station is at (lat, long) = (19.731, 204.945) and the ADCP HA1126 is at (lat, long) = (19.742, 204.930). The data from the ADCP HA1126 is depth-averaged and has removed the long period tidal measurements.

In BMP 2, simulations are controlled from the time series of offshore simulated water surface elevation located at (lat, long) = (19.758, 204.930). This point is called "Control Point" in the study. The time series of Control Point is given in Figure 4.9.

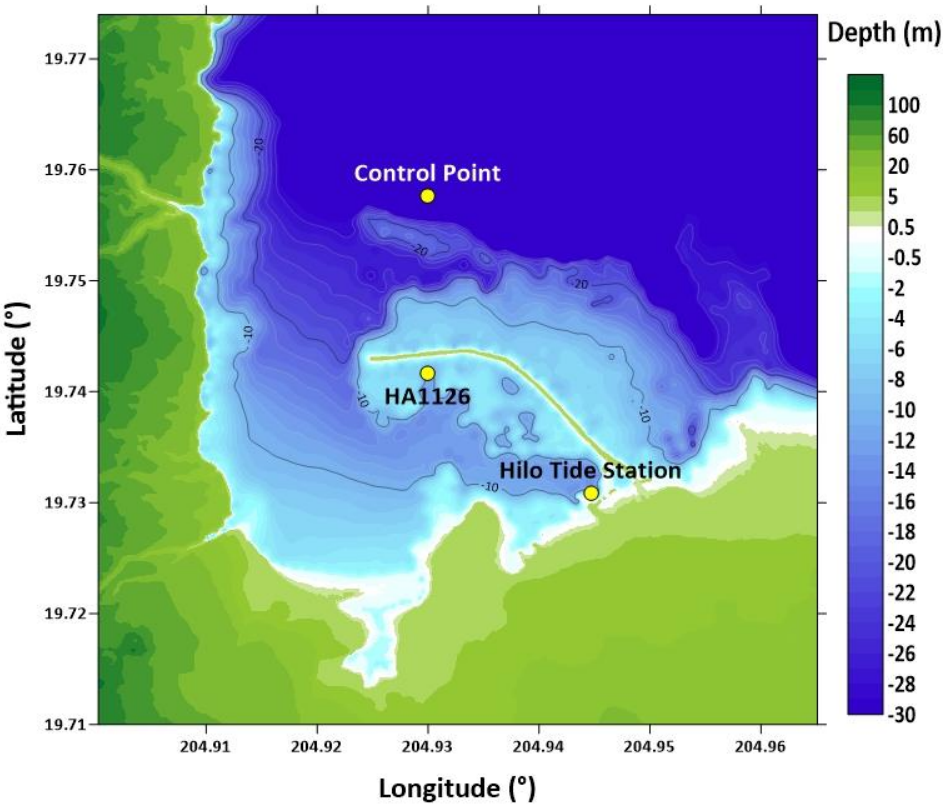

Figure 4.8 The bathymetry of Hilo Harbor provided by NTHMP

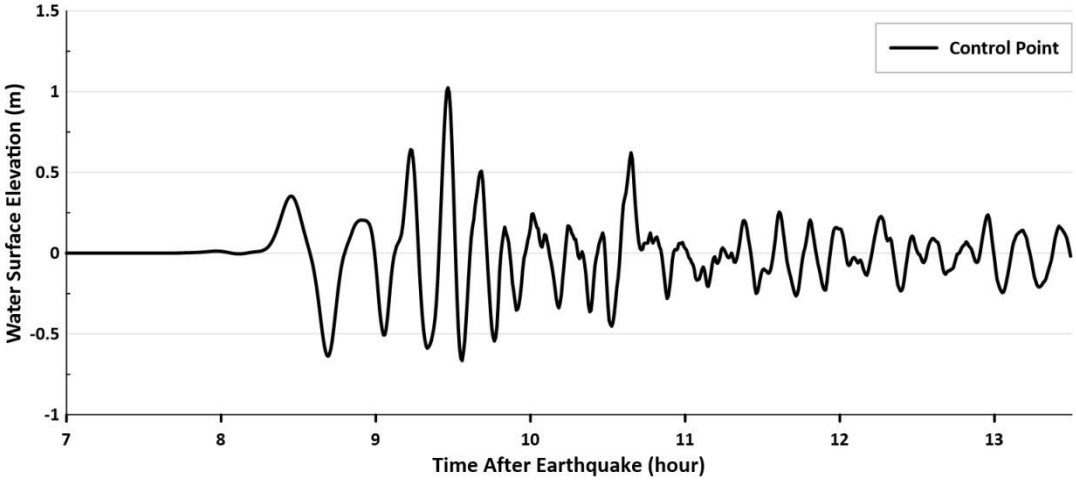

Figure 4.9 The Incident Wave (Time Series of Water surface Elevation) at Control Point, (NTHMP, 2015)

In BMP 2, the (de-tided) time series of free surface elevation from the Hilo tide station and the time series of the east-west and the north-south velocity components from the ADCP HA1126 were compared.

The simulations can proceed as either over the uppermost boundary of the grid or simulating complete case from the source to Hilo using nesting. In any case, the time series has to be checked at "Control Point" to establish offshore wave conditions properly.

In this part of the study, BMP 2 was simulated using Manning's roughness coefficient as 0.025 with a 20 m resolution. The simulation results of NAMI DANCE and DELFT3D were compared as time series at ADCP HA1126 and Hilo Tide Station. The time interval for the simulation is set as from the 7t-hour to the 13th-hour post-quake. Besides to the DELFT3D and NAMI DANCE models, Velioglu, Yalciner and Zaytsev (2016) benchmarking results with the FLOW3D model are integrated to the discussions.

The information of the grid used in simulations is given in Table 4.2.

Table 4.2 Grid information for Hilo simulations

Grid Size	356 rows x 339 columns
$\mathbf{X_{min}}$	204.90028° Easting
$\mathbf{X_{max}}$	204.96509° Easting
X Spacing	0.0001917455°
$\mathbf{Y_{min}}$	19.71° Northing
$\mathbf{Y_{max}}$	19.77398° Northing
Y Spacing	0.0001802253°

4.1.2 Application of models

Two models NAMI DANCE and DELFT3D are applied to BMP 2 and comparison of the results are given in the following sections.

4.1.2.1 Application by NAMI DANCE

The computational domain used in numerical modeling is given in Figure 4.10. The Hilo breakwater is parallel to the x-axis of the spherical coordinate system, and the incident wave propagation is perpendicular to the y axis.

Figure 4.10 3D view of Hilo Harbor NAMI DANCE computational grid

The time step is identified as 0.5 second, which meets the NAMI DANCE stability requirements with 20 m resolution of Hilo grid. Besides, the offshore incident wave time series is given as an input near the Control Point to coincide with the simulated time series to be controlled (Figure 4.11).

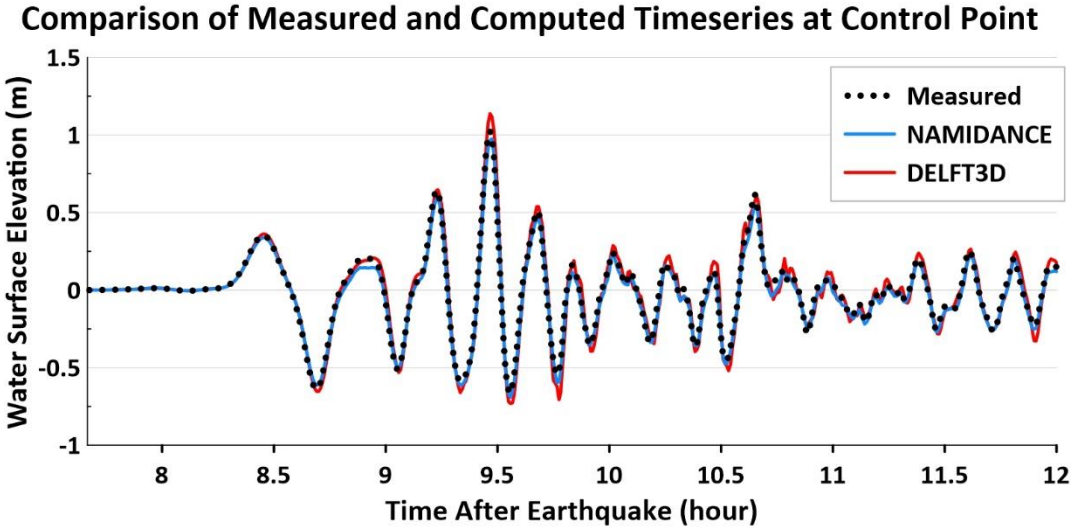

Figure 4.11 The time series of the water surface at Control Point inputted to NAMI DANCE and DELFT3D, Hilo Harbor

4.1.2.2 Application by DELFT3D

The computational grid of DELFT3D obtained from the Flow module is shown in Figure 4.12. The boundary condition for the north boundary is identified as water level time series with the incident wave. The east boundary is identified as Neumann boundary according to the DELFT3D-Flow manual. The latitude limit, y_{max} is held close to the latitude coordinate of the Control Point in order to coincide with the time series at Control Point (Figure 4.11).

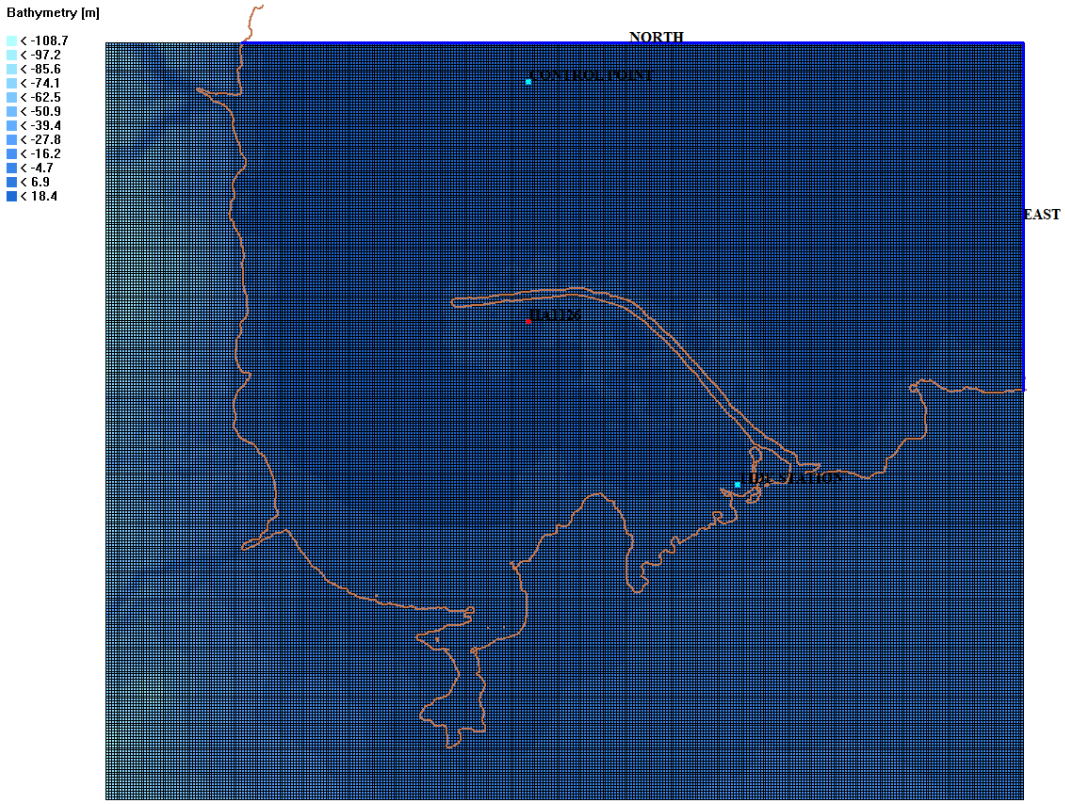

Figure 4.12 Hilo Harbor DELFT3D computational grid

4.1.3 Simulation Results and Discussions

While the propagation of the incident wave in the southward direction, it arrives the harbor from a wide opening part of the harbor and refract due to the bathymetry and diffract due to breakwater. The E-W and S-Ncomponent of water velocites are measured at ADCP HA1126 station. The water elevations are measured at Hilo Tide Station. The simulations are performed using the given time history of the water elevation at the boundary. In addition to the DELFT3D and NAMI DANCE results, Velioğlu et al. (2016) benchmarking results with the FLOW3D model is shown in the Figures 4.13 and 4.14.

Although the results show that both models follow a similar trend in terms of velocity time-series, the flow content may not be decided correctly due to the considerably low sampling interval (6 min) of the measured data even if it is

resampled. The simulated time-series are sampled as 1 sec interval for both tide station and ADCP.

The measured and computed time series of Hilo Tide Station water level elevation are showed in Figure 4.13. It is seen from the Figure that the arrival time of NAMI DANCE and DELFT3D models has a short time lag between each other; however, the wave patterns meet with the measurement at t=9 hours. On the other hand, FLOW3D and NAMI DANCE are in fairly good agreement with each other and with the measured data. Although DELFT3D time history's trend is similar to the measured data, it does not match exactly in terms of timing.

The computed velocities in the E-W and S-N components at ADCP HA1126 station are compared in Figure 4.14. It is seen from this Figure that the arrival times of the velocity components are in aggrement with the arrival time of the recorded data. In the time history of E-W velocity, FLOW3D does not fit after the time t=9.5 hour with respect to timing and gives smaller values when compared with both NAMI DANCE and DELFT3D and, with the recorded data. On the other hand, DELFT3D computes higher water levels at some intervals for the S-N component of the velocity. Also it is seen that, in the S-N velocity component figure, after time t=9.5 hour all three models' time histories starts fluctuating. It should be noted that, the reason for these fluctuations, which do not match with the recorded result, is the sampling rate. Besides, it should be noted that some peak values might be missing in the measured data due to the sampling rate of the tsunami currents.

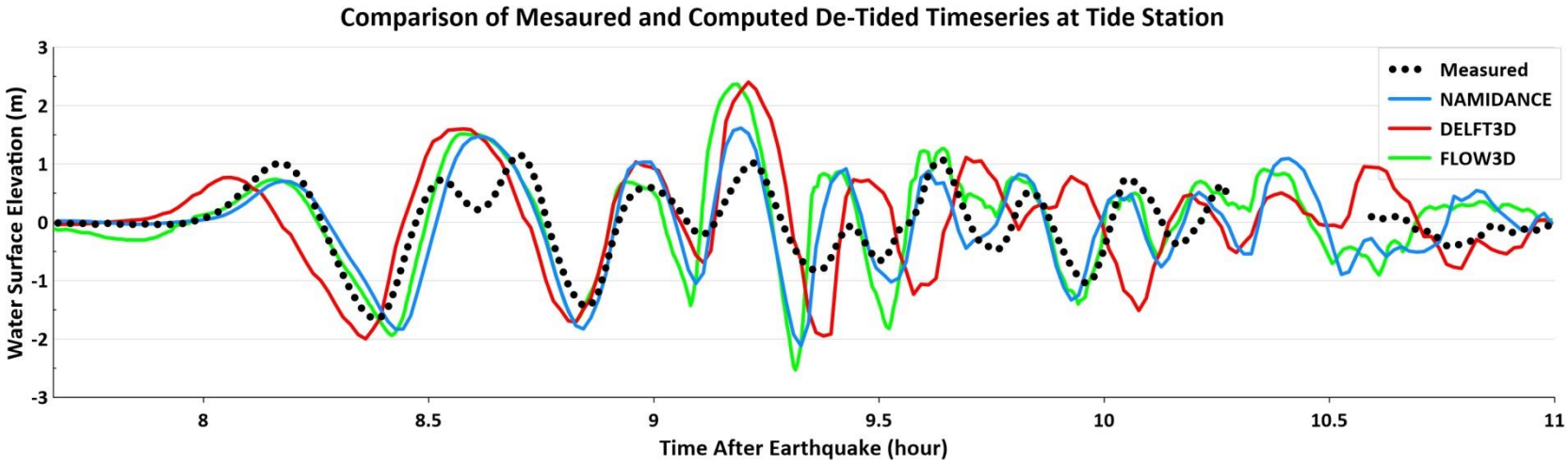

Figure 4.13 Comparison of Tide Station Timeseries, Hilo Harbor

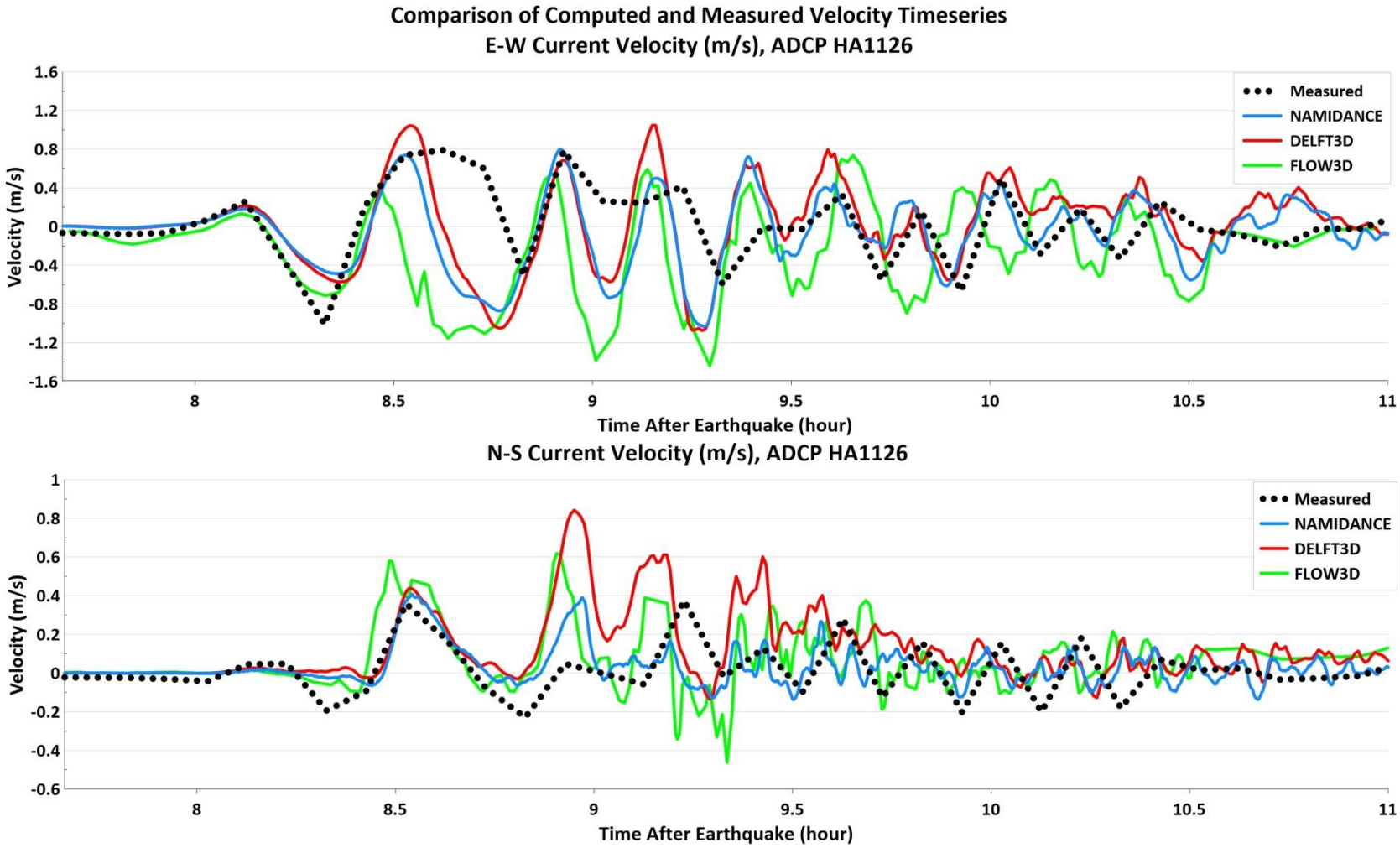

Figure 4.14 Comparison of ADCP HA1126 Current Velocity Timeseries

4.2 Benchmark Problem 4 of NTHMP: Seaside Oregon State University Model Lab

The benchmark problem 4 and the procedure to apply models are described and the computed results are presented, compared, and discuss in the following.

4.2.1 Problem Description

BMP 4 is focused on the physical model experiments (Cox et al., 2008) that examine the impact of macro-roughness elements over the flow depth of inundation, cross-shore velocity, and cross-shore momentum flux. A hydraulic model was designed by Cox et al. (2008) to study the effect of building dimensions and density on the tsunami inundation in terms of macro-roughness. The physical model of Seaside, Oregon, in the Pacific Northwest of the United States was built with a scale of 1:50. The experiments were done at Oregon State University's O.H. Hinsdale Wave Research Laboratory (HWRL) (OSU).

Several factors were considered in designing this location for research. One of them is a significant risk of tsunami in the immediate future of the Cascadia Subduction Zone (CSZ). The average length of time between CSZ disasters is 240 years, and the following case is expected to have a 7–12% chance of occurring over the next 50 years (Goldfinger et al., 2012). Another reason is the simplistic bathymetry of CSZ contours parallel to shore and a considerable onshore spit. In addition to these reasons, the concentration and location of residential and industrial structures were located well to study the predicted tsunami inundation region. (H. Park et al., 2013)

In Figure 4.15, the solid white line represents the predicted range of inundation from the tsunami event (DOGAMI, 2001). The dashed lines show the dimensions of the model and the macro-roughness of the model. The inserted map in Figure 4.15 indicates the location of Seaside, Oregon, and the Cascadia subduction zone (NOAA, 2012).

Figure 4.15 The location of Seaside, Oregon, and the physical model region (H. Park et al., 2013)

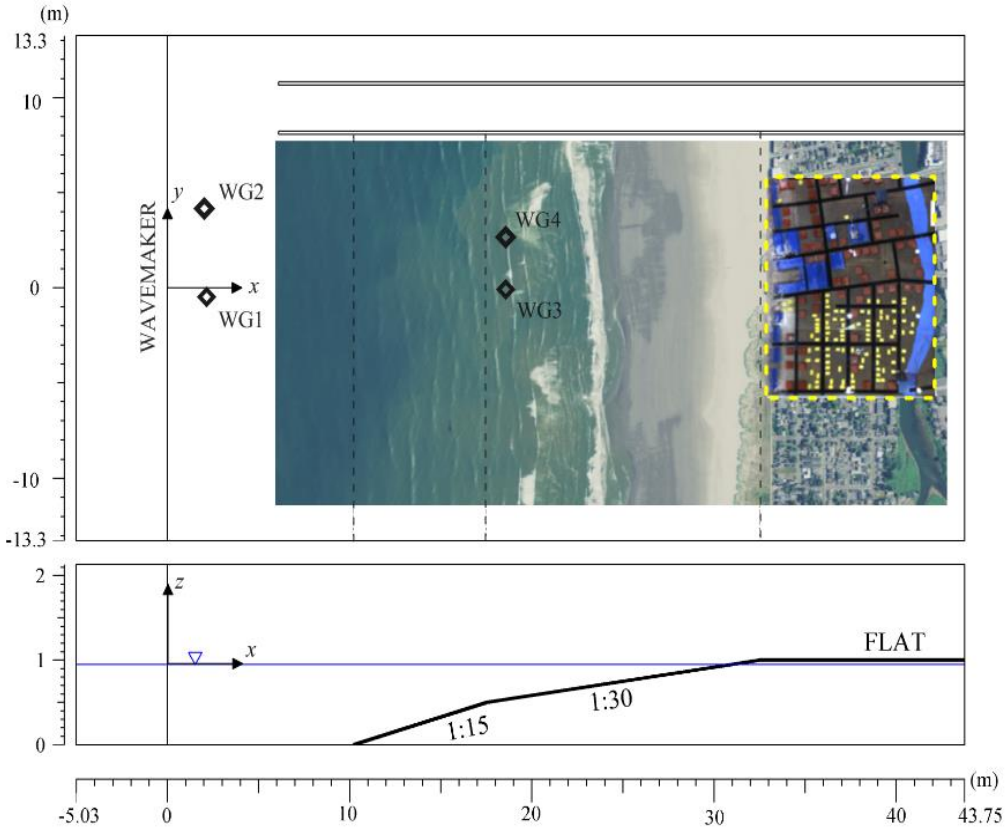

Figure 4.16 The physical model's plan and elevation view (Park et al., 2013)

The idealized bathymetry had a 10 m horizontal portion having a depth of 0.97 m near the wavemaker, an 8 m section at a 1:15 slope, a 15 m segment at a 1:30 slope where the SWL intersected, and another 11 m horizontal section extending to the back wall (Figure 4.16) (Park et al., 2013).

The sea wall along the beach with a height of 4 cm in the model is 2 m high in the actual city. The tallest building in the region is an 8-story U-shaped apartment. Other buildings are commercial buildings idealized as a square and residential buildings idealized as a smaller rectangle. The macro-roughness unit is color-coded in blue for large commercial buildings, red for smaller commercial buildings, and yellow for residences, as seen in Figure 4.17. (Park et al., 2013)

Figure 4.17 The physical model of Seaside, Oregon (Cox et al., 2008; Rueben et al., 2011).

All components were set to fix to allow for reruns of the study under the same macro-roughness parameters, and a LIDAR survey was performed to measure the position of all roughness elements (Cox et al., 2008). The Necanicum River runs through the city center nearly parallel to the shore, and the city streets were not

designed for the experiment. However, their locations were marked on the physical model, with the river painted light blue (x=42 m) and the streets painted black (Figure 4.18). Additionally, the impacts of small-scale roughness, sediments and vegetation were excluded. (Park et al., 2013)

In Figure 4.18, a total of 31 measurement locations are shown, labeled from A to D. Line A is on the streets and is numbered from 1 to 9. Lines B and C are numbered in the same way; however, the streets are inclined 10 degrees to the flow direction and are surrounded by commercial buildings. On the D line, there are four measurement points generally positioned behind the structures. (Park et al., 2013)

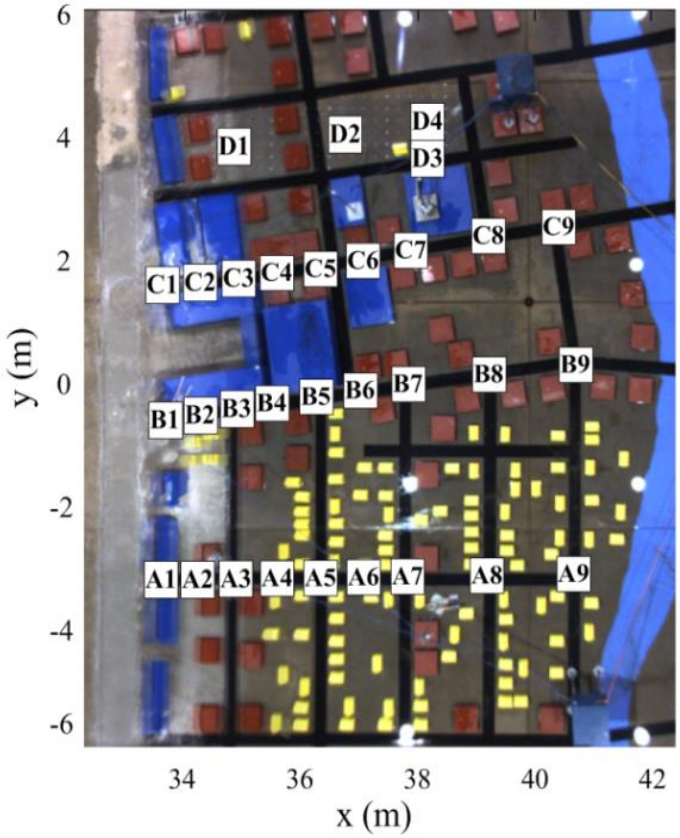

Figure 4.18 Measurement locations of the physical model (Park et al., 2013).

Cox et al. worked with optical measurement methods. Argus-cameras were placed above the basin. In order to examine the wave edge, RGB images were converted into density images. These measurements were generally accurate by about 1 cm.

Four wire resistance wave gauges (Wg), whose coordinates are given in Table 4.3, were placed in the basin. Ulta-sonic surface wave gauges and Acoustic Doppler velocimeters were placed at the coordinates given in Table 4.4 to measure the depth and velocity of the overland flow along the A, B, C and D lines.

Table 4.3 The location of Wg's in the basin

	X(m), Y(m)
Wg1	2.068, -0.515
Wg2	2.068, 4.065
Wg3	**18.618, 0**
Wg4	18.618, 2.86

Table 4.4 The location of gauges on the flat section

	USWG1/ADV1(A)		USWG2/ADV2(B)		USWG3/ADV3(C)		USWG4/ADV4(D)	
Position	X (m)	Y (m)	X (m)	Y (m)	X (m)	Y (m)	X (m)	Y (m)
1	33.611	-3.193	33.721	-0.588	33.809	1.505	35.124	3.712
2	34.103	-3.194	34.218	-0.533	34.553	1.604	36.684	3.888
3	34.534	-3.184	34.679	-0.467	35.051	1.686	38.086	4.070
4	35.040	-3.181	35.176	-0.406	35.556	1.769	38.141	3.585
5	35.544	-3.194	35.747	-0.317	36.050	1.845	N/A	N/A
6	36.355	-3.199	36.635	-0.229	37.047	1.988	N/A	N/A
7	37.767	-3.201	37.773	-0.068	38.243	2.193	N/A	N/A
8	39.223	-3.204	39.218	0.135	39.208	2.338	N/A	N/A
9	40.676	-3.228	40.668	0.269	40.400	2.582	N/A	N/A

As a result of the study, it was observed that macro roughness significantly reduced the spreading rate along the waterfront and in building areas. Hydraulic jumps were observed in narrow-spaced macro-roughness areas. In contrast to open streets parallel to flow direction, the flow was delayed in regions with macro roughness.

This analysis suggests that macro-roughness components significantly impact the tsunami inundation mechanism as opposed to areas devoid of macro-roughness. The macro roughness components result in a 40% reduction in the speed of

inundation. Additionally, the properties of macro-roughness features have a significant result on tsunami inundation (Rueben et al., 2011).

Cox et al.'s (2008) experiment produced a large dataset in the aspect of computational models for laboratory benchmarking. Figure 4.19 illustrates the suggested numerical simulation domain for modelers in Benchmark Problem 4 of NTHMP (National Tsunami Hazard Mitigation Problem) - Mapping and Modeling Benchmarking Workshop.

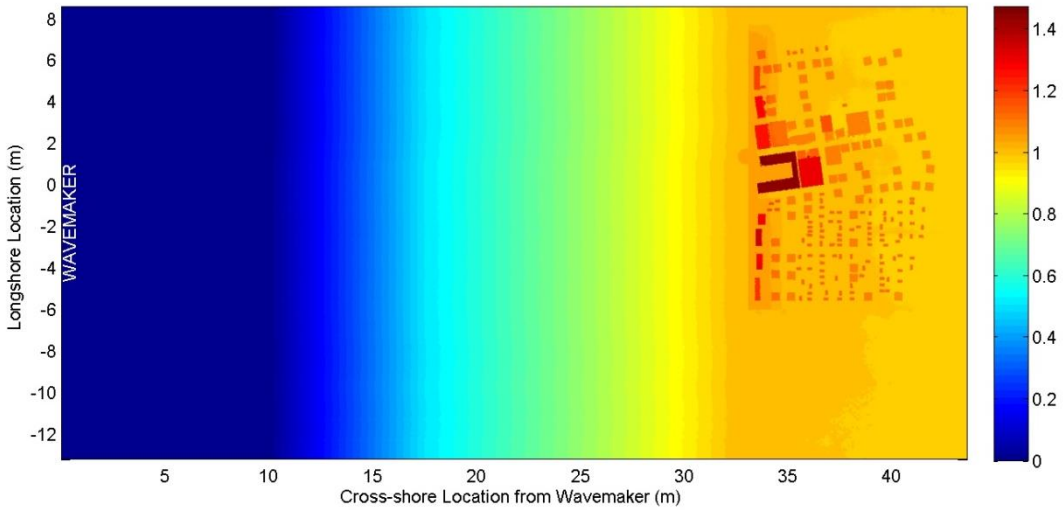

Figure 4.19 The bathymetry for BMP 4

BMP 4 is simulated by using time history of water elevation at WG3 as input. The overland flow depth, cross-shore velocity, and cross-shore specific momentum flux are computed at the gauge locations B1, B4, B6 and, B9 for comparison with the measurement.

4.2.2 Application of Models

The bathmetry and the locations of the gauge points B1, B4, B6 and B9 are shown in Figure 4.20.

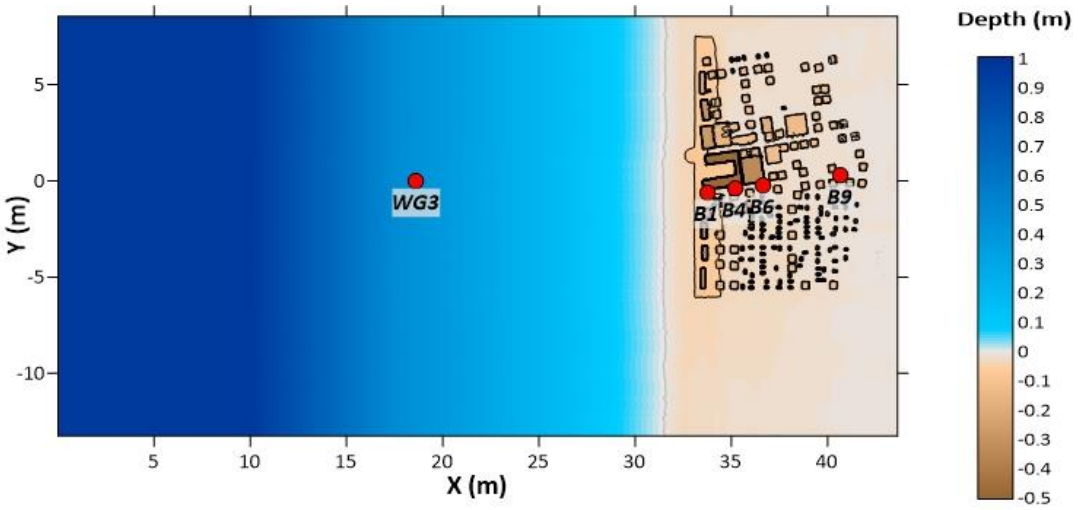

Figure 4.20 The computational domain of BMP4

The grid resolution is selected as 0.1 m, as recommended by BMP4. The time step is set as 0.001 second, which meets the stability criterion for both models. Another time steps are also examined; nevertheless, no substantial difference is found. The coefficient of Manning's roughness is taken as 0.01 depending on the recommendation of Park et al. (2013).

BMP 4 is simulated by using time history of water elevation at WG3 as input (Figure 4.21).

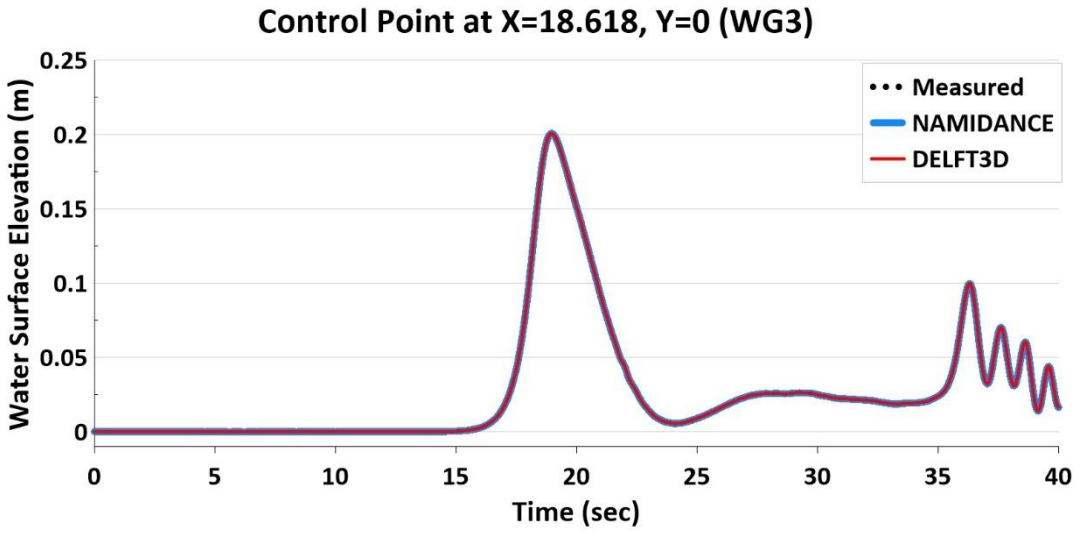

Figure 4.21 The input time series at Control Point WG3

The 3D view of the numerical domain used in the NAMI DANCE run is shown in Figure 4.22. To prevent outflow from the computational region, boundaries are set as rigid walls at y_{min} and y_{max}.

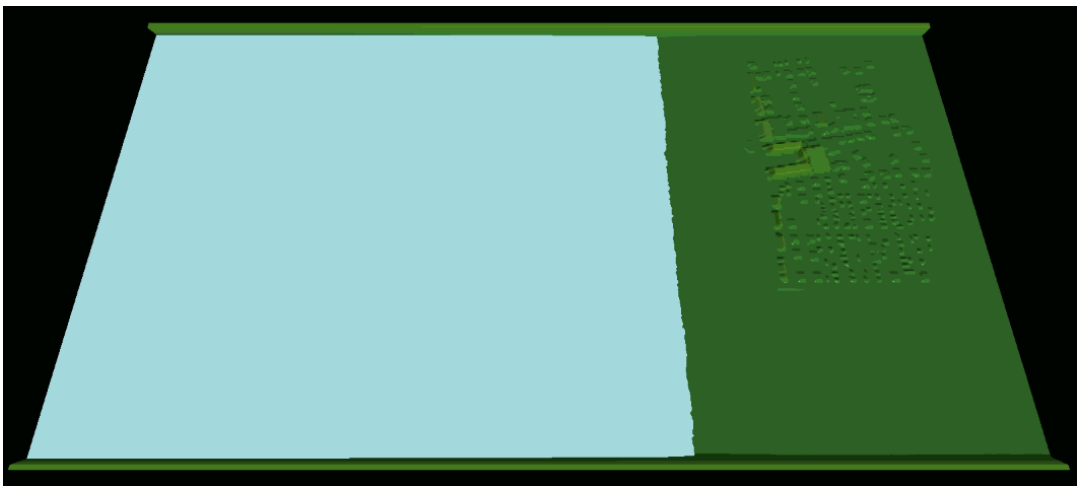

Figure 4.22 3D view of the study domain plotted by NAMI DANCE

The computational domain of the physical experiment conducted by Cox et al. (2008) used in the DELFT3D simulation is shown in Figure 4.23.

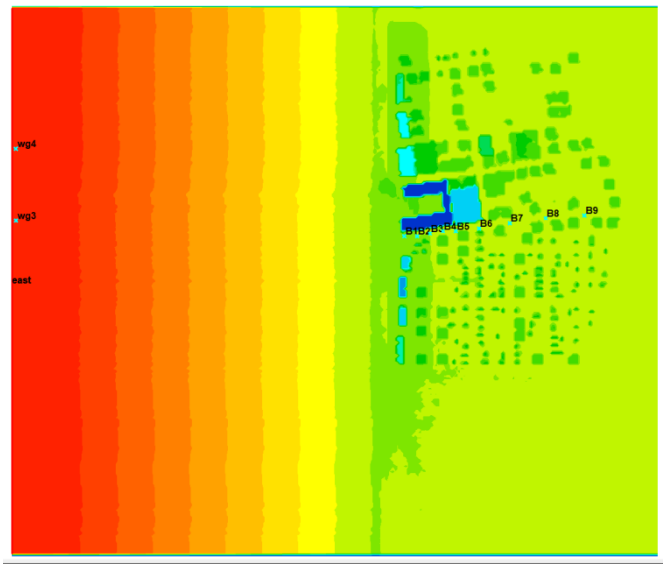

Figure 4.23 Top view of the study domain used in the simulation by DELFT3D

4.2.3 Simulation Results and Discussions

In addition to the results of DELFT3D and NAMI DANCE numerical models, the results of FLOW3D numerical model (Velioglu, Yalciner and Zaytsev, 2016) are are also used in the comparisons and discussions.

The simulations are performed by using time history of water elevation at WG3 as input and the time series of overland flow depth, cross-shore velocity, and cross-shore momentum flux at the locations B1, B4, B6, and B9 are computed and given in Figures 4.24, 4.25, and 4.26, respectively.

When the results are compared, the computed time histories of these parameters are in aggrement between three models and the measurements (Figure 4.24). At the location B1, the arrival time of the wave is earlier (less than a second) in NAMI DANCE results and FLOW3D underpredictes around the first arrived waves. On the other hand, in DELFT3D results, the time history of overland flow depth meets with the measured data with respect to arrival time and the trend gives more coherence than other two models At the location B4, after the first peak of the flow depth, all three models and the measurement data fit at the same results. At the location B6, NAMI DANCE results meet with the experimental results with respect to the arrival time. However, DELFT3D results arrive late to B6. The wave does not reach B9 in 40 seconds simulation time of DELFT3D. It is noted that FLOW3D computed comparable results at point B9. The experimental results show that the maximum flow depth decreases from 0.22 m at B1 to 0.044 m at B9. The maximum flow depth at location B1 is about 0.17 m for NAMI DANCE and DELFT3D models and 0.14 m for FLOW3D model. In addition, at B9, the maximum flow depth decreases to 0.02 m in the NAMI DANCE run and to 0.024 m in FLOW3D result while the wave does not reach B9 in 40 sec in the DELFT3D run. As expected, the flow depth decreases as the wave propagates into the macro roughness area.

The experimental maximum cross-shore velocity is 2 m/s at B1 and 1.4 m/s at B9 (Figure 4.25). The cross-shore velocity decreases from 2.16 m/s at B1 to 0.55 m/s at the B9 location in the NAMI DANCE simulation and from 1.54 m/s at B1 to 0.73 m/s at B9 location in the FLOW3D result. FLOW3D cross-shore velocity time histories meet with the measurements at the locations B1 except the drop at time t≈29 sec, B4, B6, and B9 after the time t≈33 sec. Similarly, in DELFT3D, the maximum velocity is 1.5 m/s at B1 and 0.98 m/s at B6. DELFT3D underestimes the cross-shore velocity for all four locations.

With respect to the cross-shore momentum flux (Figure 4.26), the experimental maximum value drops from 0.96 m3/s2 at B1 to 0.034 m3/s2 at B9. In the NAMI DANCE simulation, the cross-shore momentum flux drops from 0.8 m^3/s^2 at B1 to 0.011 m^3/s^2 at B9 location. Except from the arrival time at B1 and B4 location, the computed time history of the cross-shore momentum flux by NAMI DANCE fits with the experimental results at the locations B1, B4, and B6. The maximum values of momentum flux decreases from 1.1 m^3/s^2 at B1 to 0.36 m^3/s^2 at B6 in DELFT3D simulation and from 0.27 m^3/s^2 at B1 to 0.009 m^3/s^2 at B9 location in FLOW3D simulation. Besides, FLOW3D results at the location B1 and B4 underestimes when compared with the results of the experiment and other two models. In addition DELFT3D overestimes the cross-shore momentum flux at the locations B1 and B4.

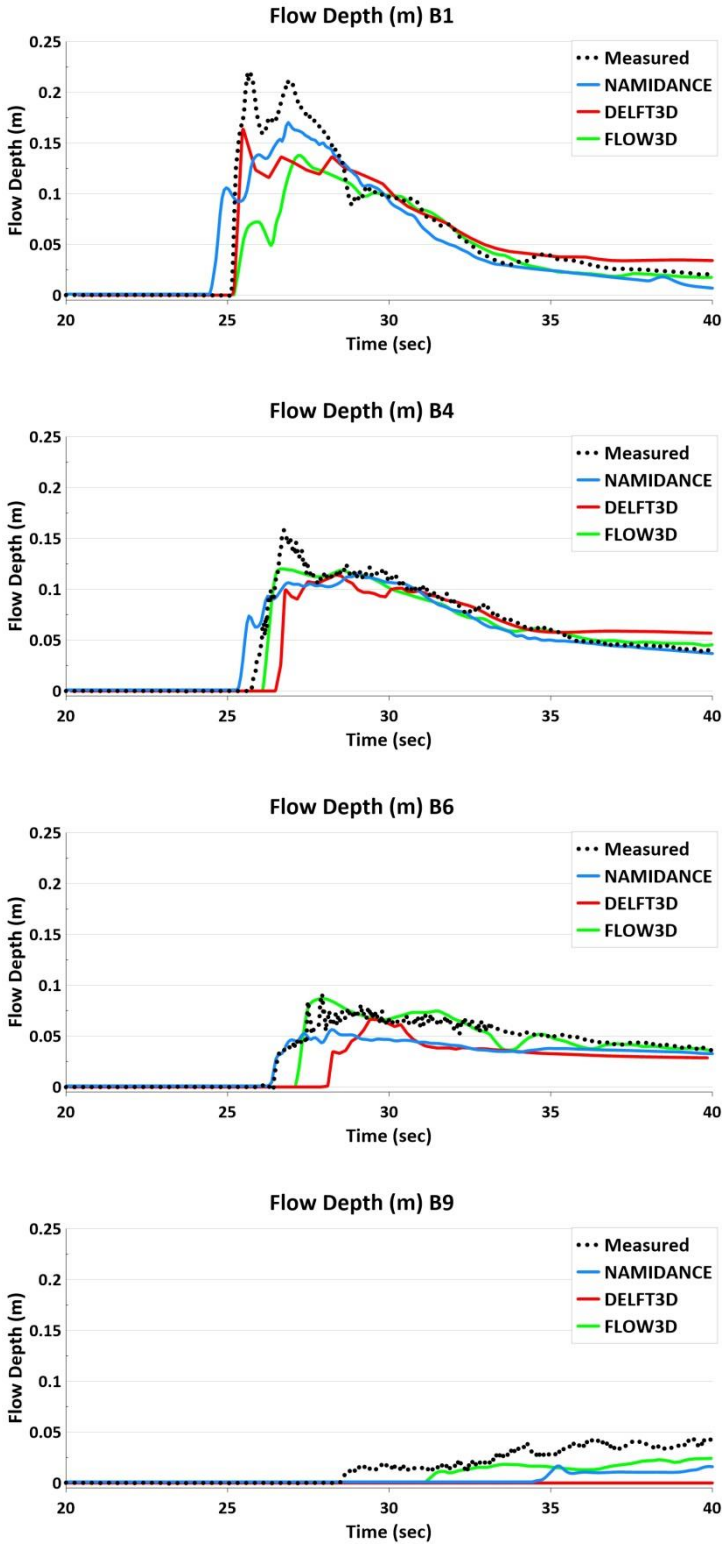

Figure 4.24 Comparison of measured and computed overland flow depth at B1, B4, B6, and B9 respectively

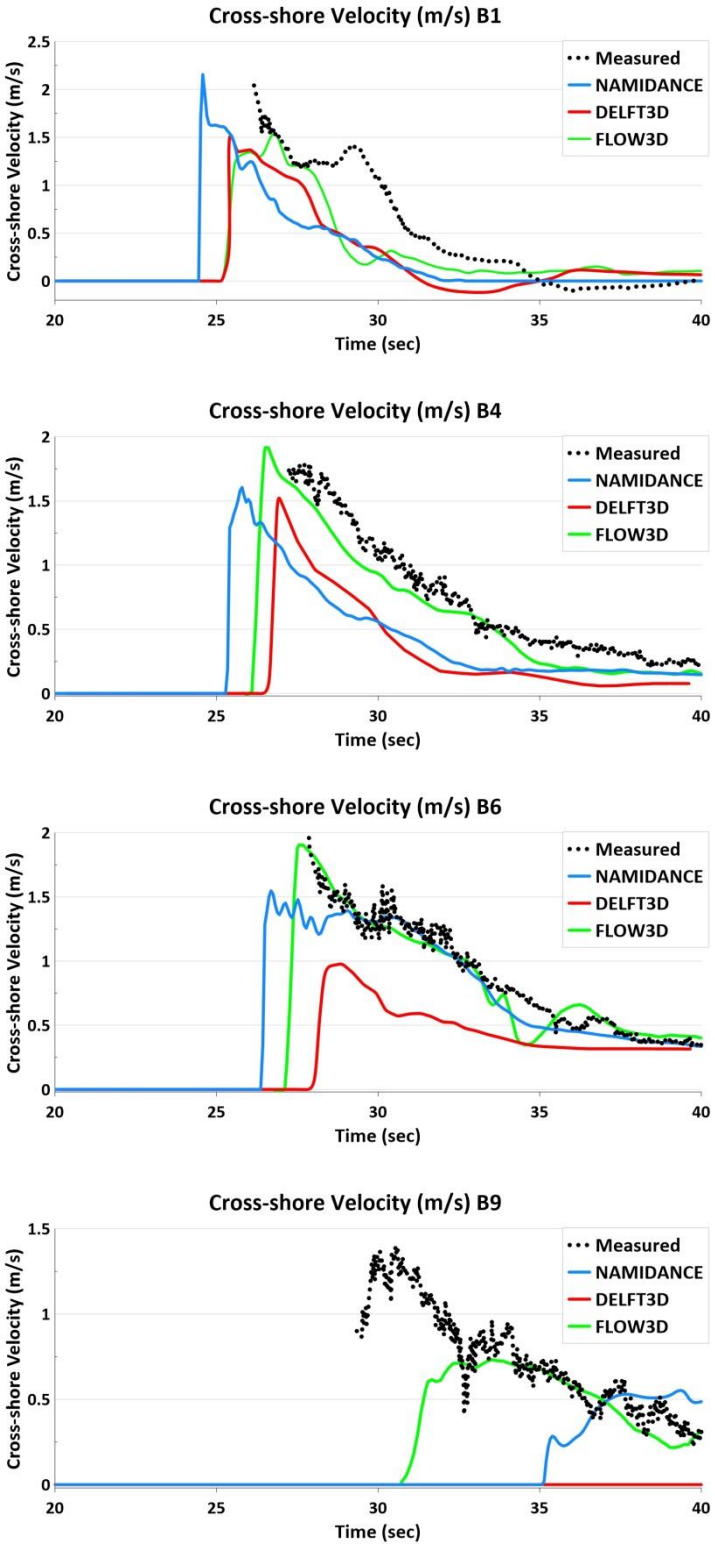

Figure 4.25 Comparison of measured and computed cross-shore velocity at B1, B4, B6, and B9 respectively

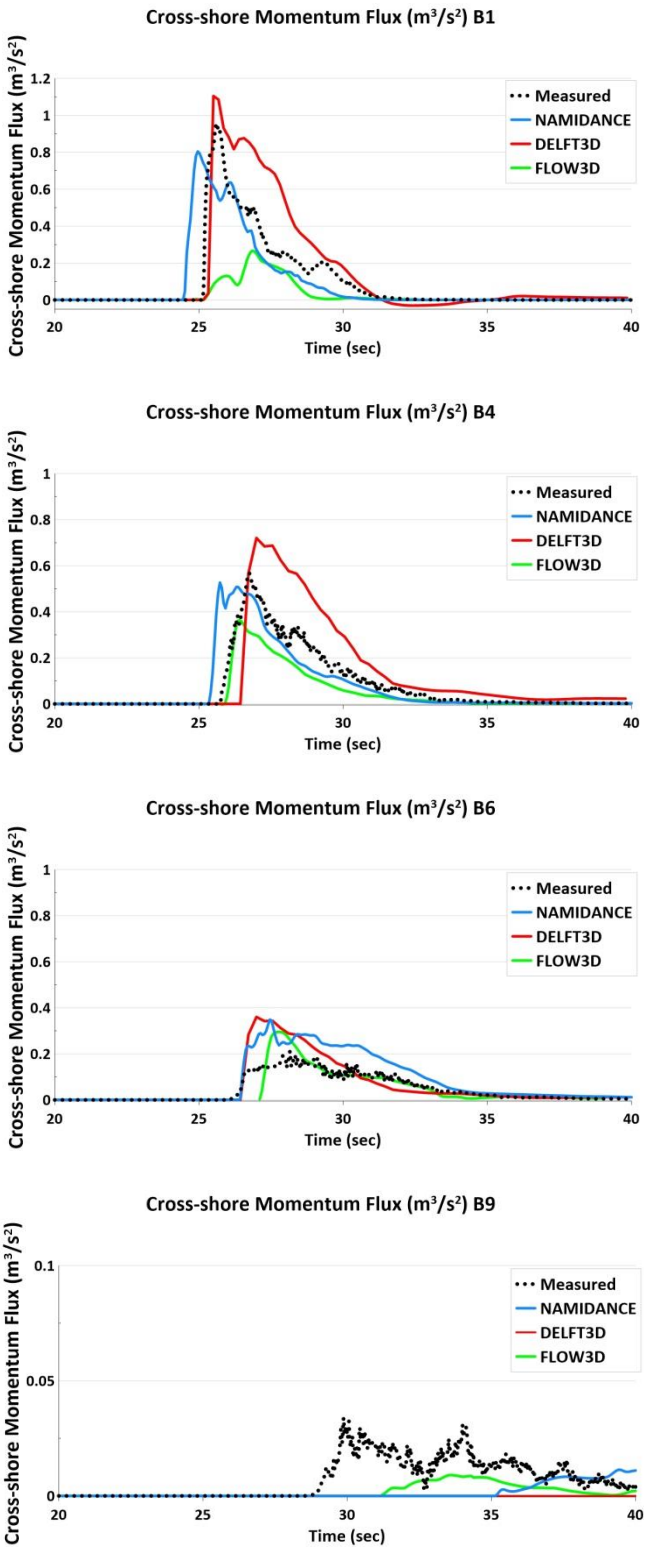

Figure 4.26 Comparison of measured and computed cross-shore momentum flux at B1, B4, B6, and B9 respectively

CHAPTER 5

CASE STUDY APPLICATION TO TROPICAL CYCLONE DORIAN 24 AUGUST - 7 SEPTEMBER 2019

Tropical cyclone Dorian is studied as a case study in order to test NAMI DANCE tropical cyclone module by comparing the numerical results with observations and records. Problem description, application of NAMI DANCE numerical model and the computed results are presented in the following sections with the comparison and discussions.

5.1 Event Description

The tropical wave that formed on the west coast of Africa on 19 August 2019 moved westward across the tropical Atlantic, but storm activity was decreasing in the meantime. Later, the cyclonic circulation observed from the satellite showed that a convection field developed again around 40° West on 22 August. On August 24th, this energy turned into a tropical depression, then a tropical storm. The path of the Tropical Cyclone Dorian is shown in Figure 5.1 (NOAA, National Hurricane Center, 2020)

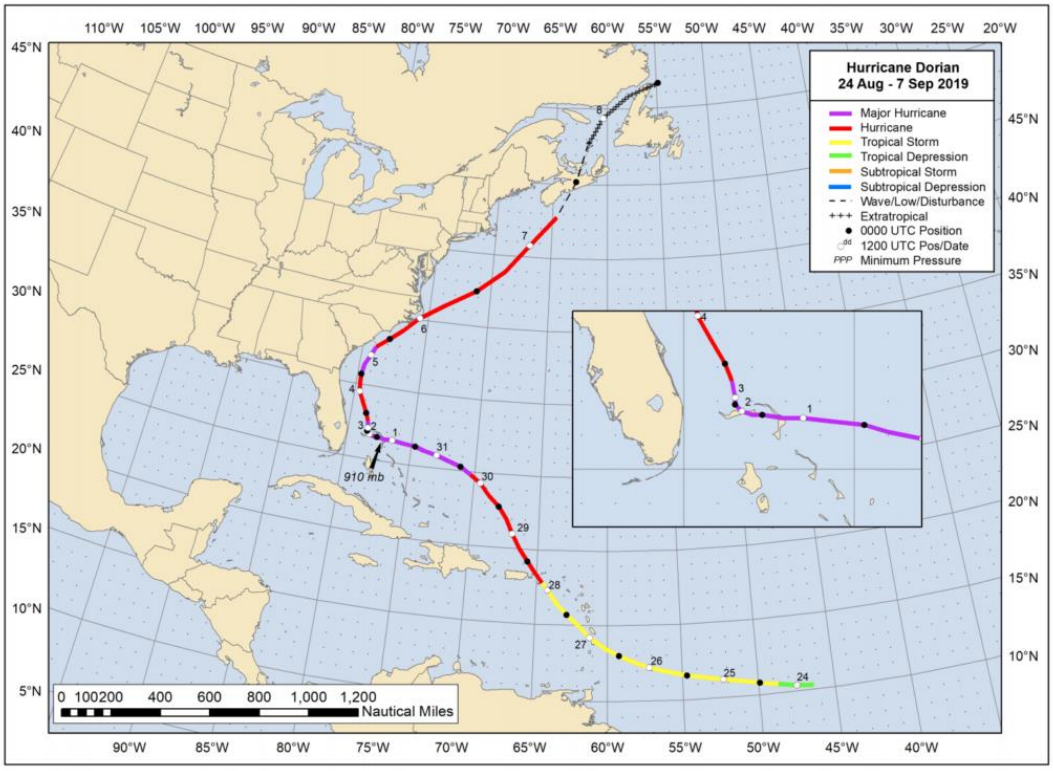

Figure 5.1 Best track of Tropical Cyclone Dorian (NOAA, National Hurricane Center, 2020)

At 16:40 UTC on 1 September, Dorian had become a category five Tropical Cyclone with predicted winds of 160 kt (~296 km/h) and a minimum pressure of 91000 Pa (Figure 5.2 and Figure 5.3).

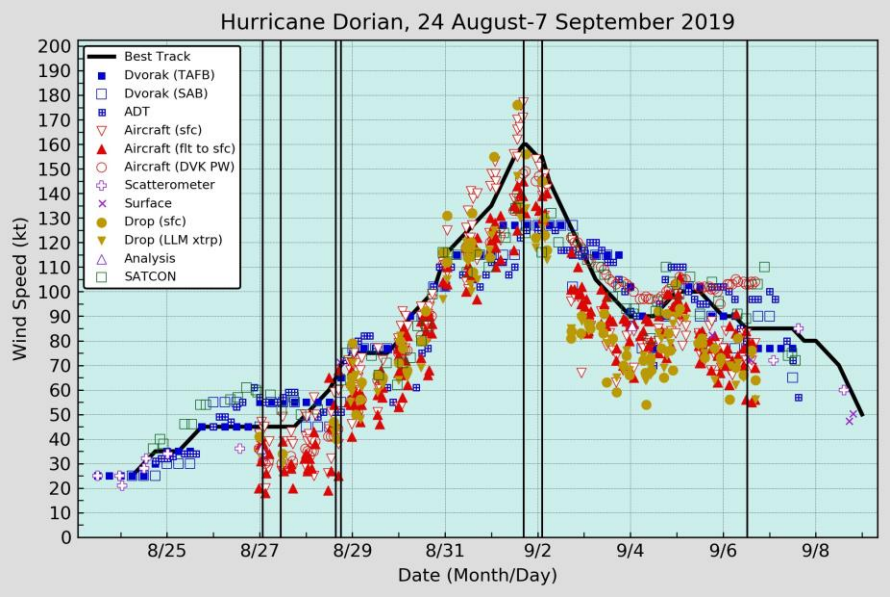

Figure 5.2 The observations of wind speed with the best track, Tropical Cyclone Dorian (NOAA, National Hurricane Center, 2020)

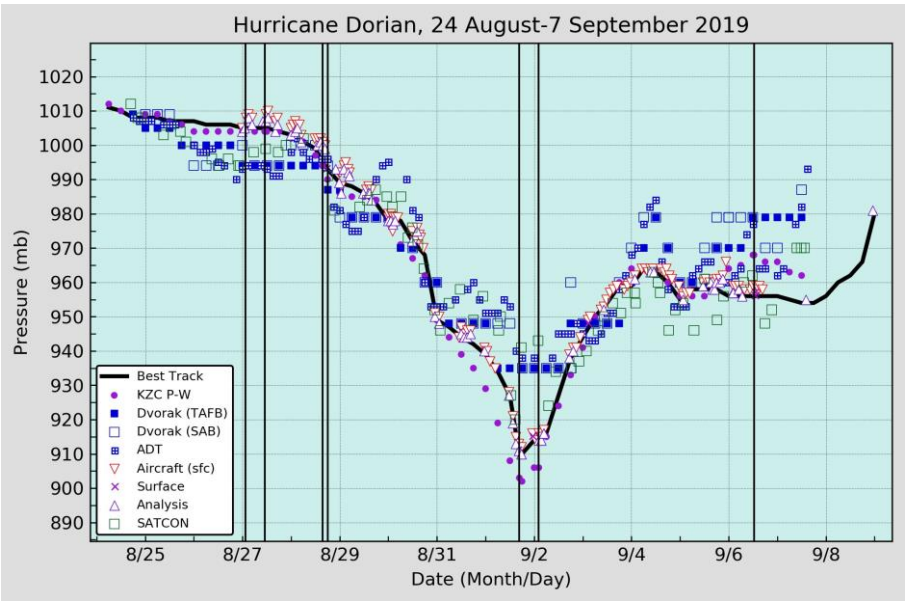

Figure 5.3 The observations of central pressure with the best track, Tropical Cyclone Dorian (NOAA, National Hurricane Center, 2020)

The region Tropical Cyclone Dorian damaged the most was Bahamas other than United States and Canada. In Dorian, more than 200 people are considered as lost their lives, according to The Health Minister, in Bahamas. The Bahamas Weather Service estimated the total at 74 (63 in Abaco and 11 in Grand Bahama). Also, it is reported that the number of missing people was 245. Besides, more than 75 percent of the houses were damaged extensively (Figure 5.4) (NOAA, National Hurricane Center, 2020).

Figure 5.4 Extensive damage on the northwest Bahamas (NOAA, National Hurricane Center, 2020)

Tropical Cyclone Dorian generated a storm surge affecting U.S. Virgin Islands, Puerto Rico, Bahamas, Florida, Georgia, South Carolina, North Carolina, Virginia, damaged coastal areas with inundation and storm surge flooding. The measurement water level was 1.95 m above Mean Higher High Water sea level at the tide gauge of the University of Hawaii Sea Level Center (UHSLC) on the Grand Bahama Islands. On Grand Bahama Island and the Abaco Islands, higher water levels occurred farther east. However, there are no measurements of the tide gauge available from those areas.

In the Hampton Roads area of Virginia, inundation levels of 0.6 m to 0.9 m above ground level occurred north of North Carolina. At the Chesapeake Bay entrance, the NOS tide gauge measured a maximum water level of 1 m MHHW, and a maximum water level of 0.95 m MHHW was recorded by a gauge at Sewells Point in Norfolk, Virginia.

5.2 Application of Model

Tropical Cyclone Dorian is simuated by NAMI DANCE by inputting spatial and temporal changes of wind fields and pressure fields before, during and after the cyclone from 31 August 2019 to 7 September 2019. The large Domain (Figure 5.5) is selected covering the cyclone path from the start to the end of the cyclone. Grid information of large domain is given in Table 5.1. Inside the large domain two different smaller (Nested-1 and Nested-2) domains are selected (Figure 5.6). The Nested-1 domain covers the Bahamas region where the most hit of the cyclone are observed. The Nested-2 domain is selected to cover the region where National Ocean Service stations are located, and the water level change has been recorded at those stations. Therefore, the results of NAMI DANCE in the simulation for Nested-1 can be compared with the observations in Bahamas and for Nested-2 can be compared with the water level measurements at the stations. Grid information of Nested-1 and Nested-2 domains used in the simulations are given in Table 5.2. The

bathymetry data is obtained from a free source GEBCO (General Bathymetric Chart of the Oceans) https://www.gebco.net/.

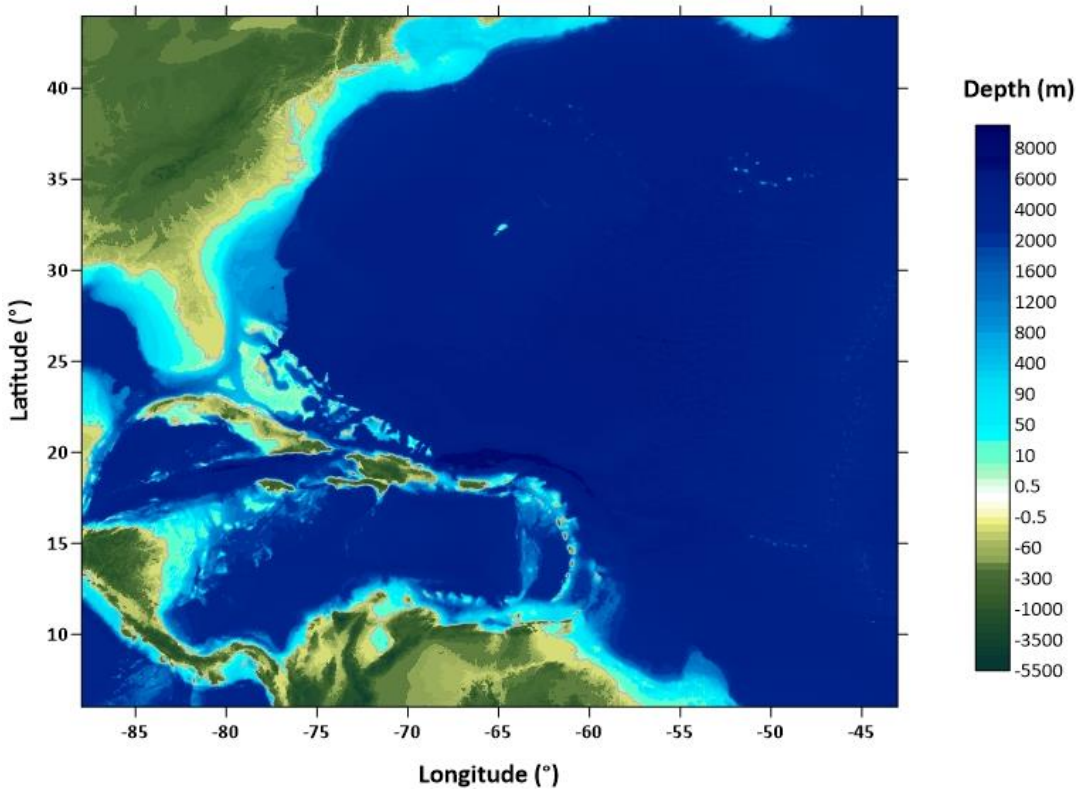

Figure 5.5 Large domain for Tropical Cyclone Dorian simulations

Table 5.1 Grid information of large domain for tropical cyclone Dorian simulations

Grid size	570 rows x 675 columns
X_{min}	-87.96666° Easting
X_{max}	-43.03333° Easting
X Spacing	0.06666°
Y_{min}	6.03333° Northing
Y_{max}	43.96666° Northing
Y Spacing	0.06666°

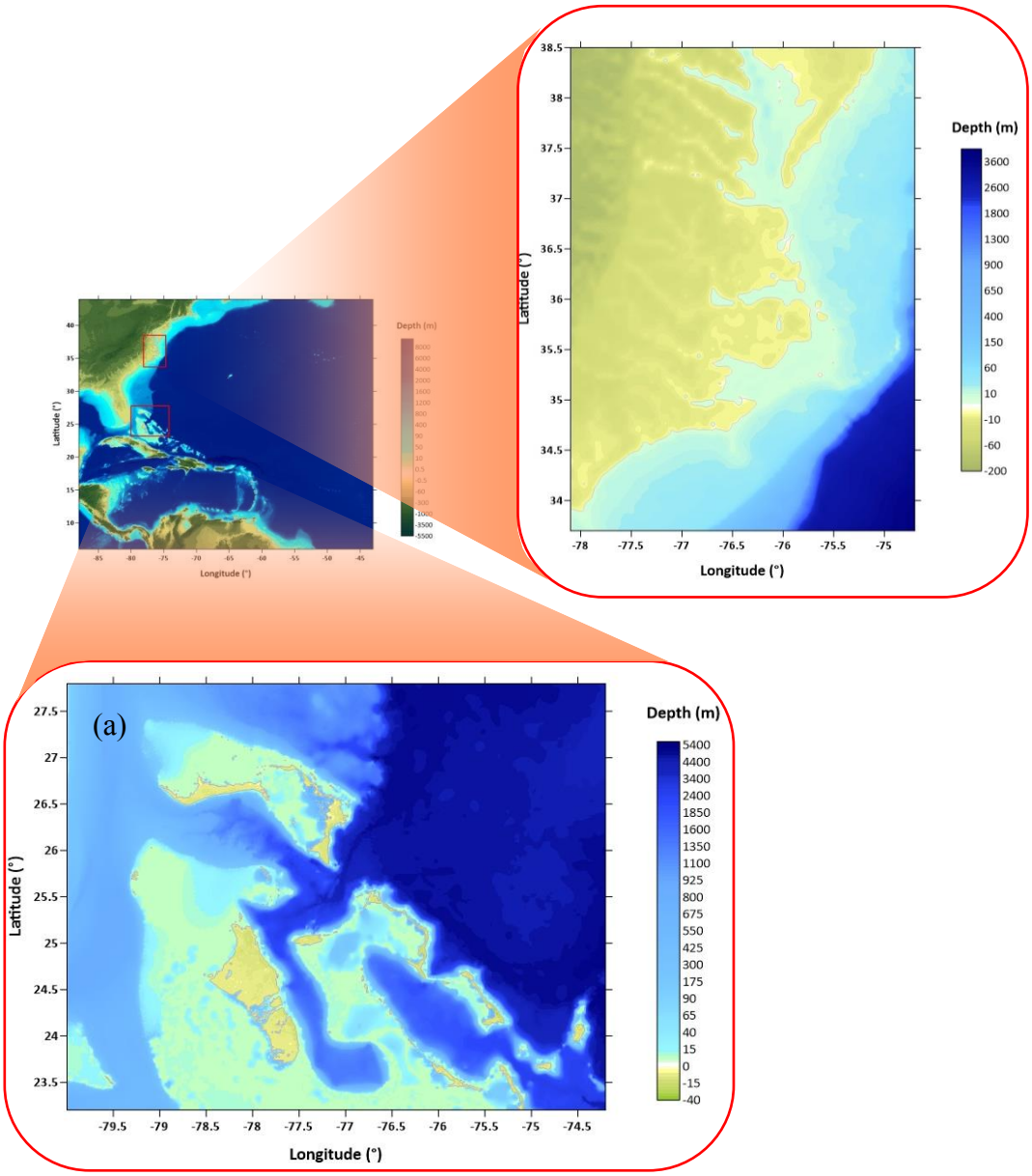

Figure 5.6 Nested-1 (a) and Nested-2 (b) domains for Tropical Cyclone Dorian simulations

Table 5.2 Grid information of Nested-1 and Nested-2 domains for the simulations

	Nested-1	**Nested-2**
Grid Size	1104 rows x 1392 columns	1201 rows x 851 columns
$\mathbf{X_{min}}$	-79.99792° Easting	-78.1° Easting
$\mathbf{X_{max}}$	-74.20228° Easting	-74.7° Easting
X Spacing	0.00417°	0.004°
$\mathbf{Y_{min}}$	23.20208° Northing	33.7° Northing
$\mathbf{Y_{max}}$	27.79792° Northing	38.5° Northing
Y Spacing	0.00417°	0.004°

As mentioned before, the Nested-1 area has no tide station inside. The reason why that location is selected is that it is known that Bahamas got maximum damaged in this tropical cyclone.

Besides, for Nested-2 gauge, points are selected at coordinates of National Ocean Service stations. The gauge locations are presented on Figure 5.7 for Nested-1 and Figure 5.8 for Nested-2 domain.

The reported extremes of pressure, storm surge levels, and wind are tabulated in Table 5.3 for the selected NOAA stations.

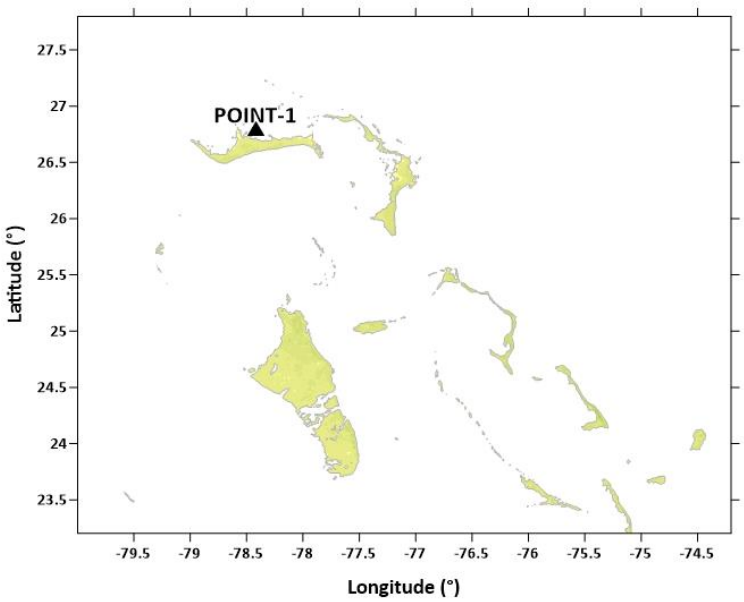

Figure 5.7 Gauge points of Nested-1 domain for Tropical Cyclone Dorian simulations

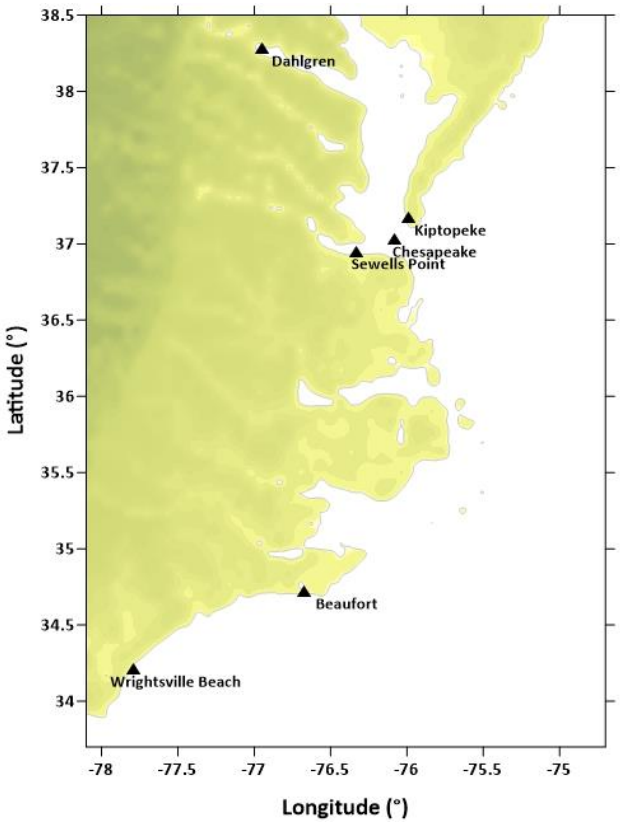

Figure 5.8 Gauge points of Nested-2 domain for Tropical Cyclone Dorian simulations

Table 5.3 The maximum values of pressure, storm surge and, wind for choosen stations reported by NOAA, NHC

Location	Minimum Sea Level Pressure		Maximum Surface Wind Speed		Storm Surge (m)
	Date/time (UTC)	Pressure (kPa)	Date/time (UTC)	Gust (km/h)	
Beafort (34.72N 76.67W)	06/08:18	97.050	06/08:42	118	0.63
Wrightsville Beach (34.21N 77.79W)	06/04:12	98.360	06/02:48	111	0.62
Sewells Point (36.95N 76.33W)	06/13:36	100.040	-	-	1.09
Kiptopeke (37.17N 75.99W)	-	-	06/15:42	78	0.9
Dahlgren (38.32N 77.04W)	06/19:48	100.610	-	-	0.62
Chesapeake Channel BBT (37.03N 76.08W)	06/15:06	99.700	06/15:00	107	1.1

Along with the maximum values, there are stations' data as time series. However, it should be noted that observed water level values of NOAA stations include the level of storm surge due to pressure and wind and other factors such as wind setup, wave set up, wave run-up, and tide also.

5.2.1 Application by NAMI DANCE

The computaional domian of NAMI DANCE model is shown below in Figure 5.9.

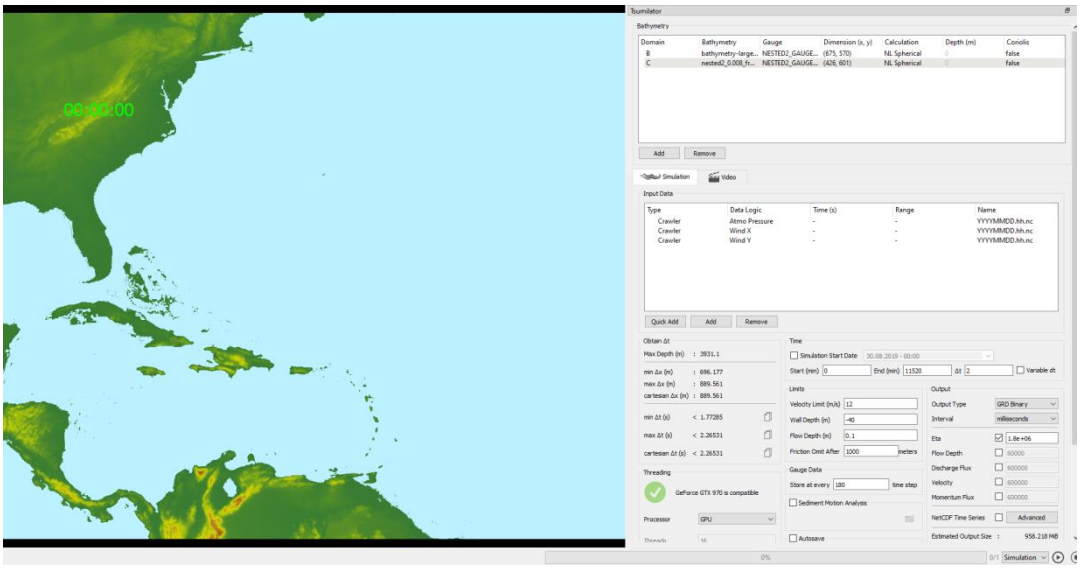

Figure 5.9 NAMI DANCE simulation domain for Tropical Cyclone Dorian

The time step is chosen as 2 seconds with the provision of NAMI DANCE stability conditions. In addition, manning's roughness coefficient is taken as 0.02 with respect to Mattocks and Forbes, 2008.

5.3 Meteorological Input Data

The European Centre for Medium Range Weather Forecasts (ECMWF) High-Resolution Forecast (HRES) data being an open source were used as meteorological data, namely, mean sea level pressure and wind data above 10 m high of sea level with 9 km resolution grid and 6-hour time interval with 1-hour forecast. It is decided to continue with HRES data after comparison of Climate Forecast System Reanalysis (CFSR) and ECMWF Re-Analysis 5 (ERA5) data. Tropical cyclone Dorian was simulated from 30 August 2019 to 7 September 2019 (8 days).

The minimum mean sea level pressure is 98000 Pa at 06 Sep 23:00, according to HRES data (Figure 5.10). Figure 5.10 also shows wind data at 06 Sep 23:00 in east-west (u) and sorth-nouth (v) directions.

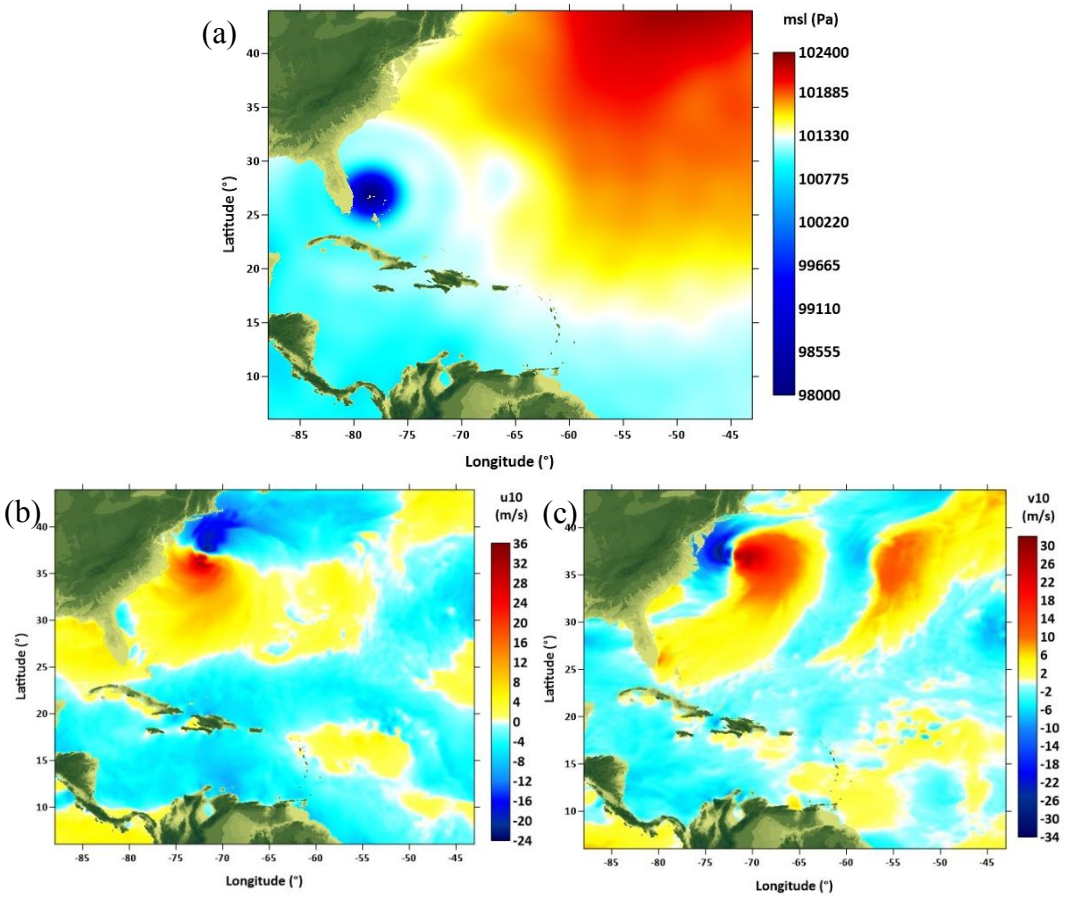

Figure 5.10 The minimum mean sea level pressure of HRES (a) and the wind in u direction (b) and in v direction (c) of the same time (6 Sep 23:00)

The ECMWF HRES dataset is shown with the 12 hours time interval for the coarse domain in the Appendix section.

5.4 Simulation Results and Discussions

The simulation is performed using the meteorological (spatial and temporal change of pressure and wind field) data from 30 August 2019 to 7 September 2019. The time-series of water level computed by NAMI DANCE and comparison with the recorded data are given in Figure 5.11.

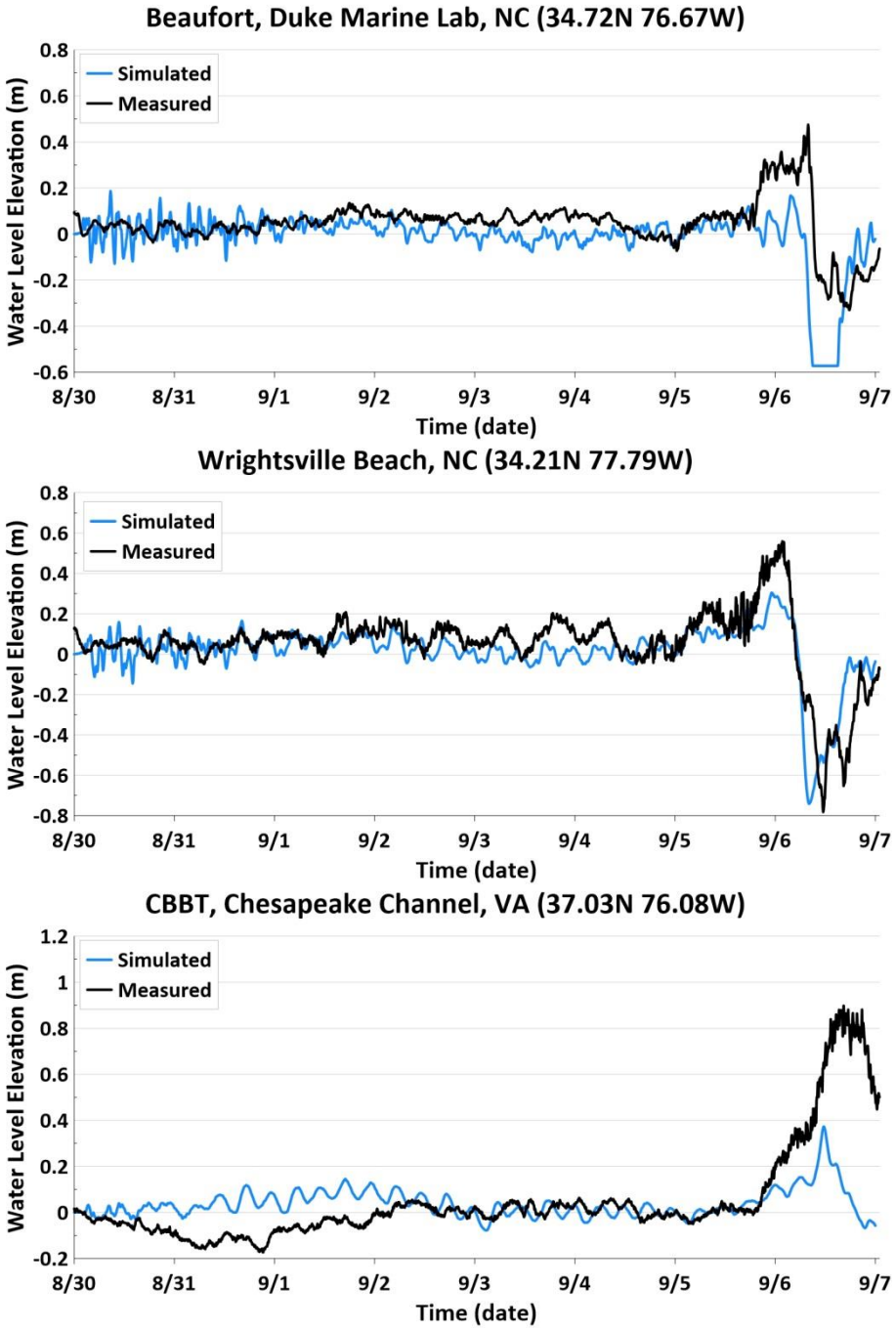

Figure 5.11 Comparison of simulated and recorded water level time-series of stations

Fig. 5.11 cont'd.

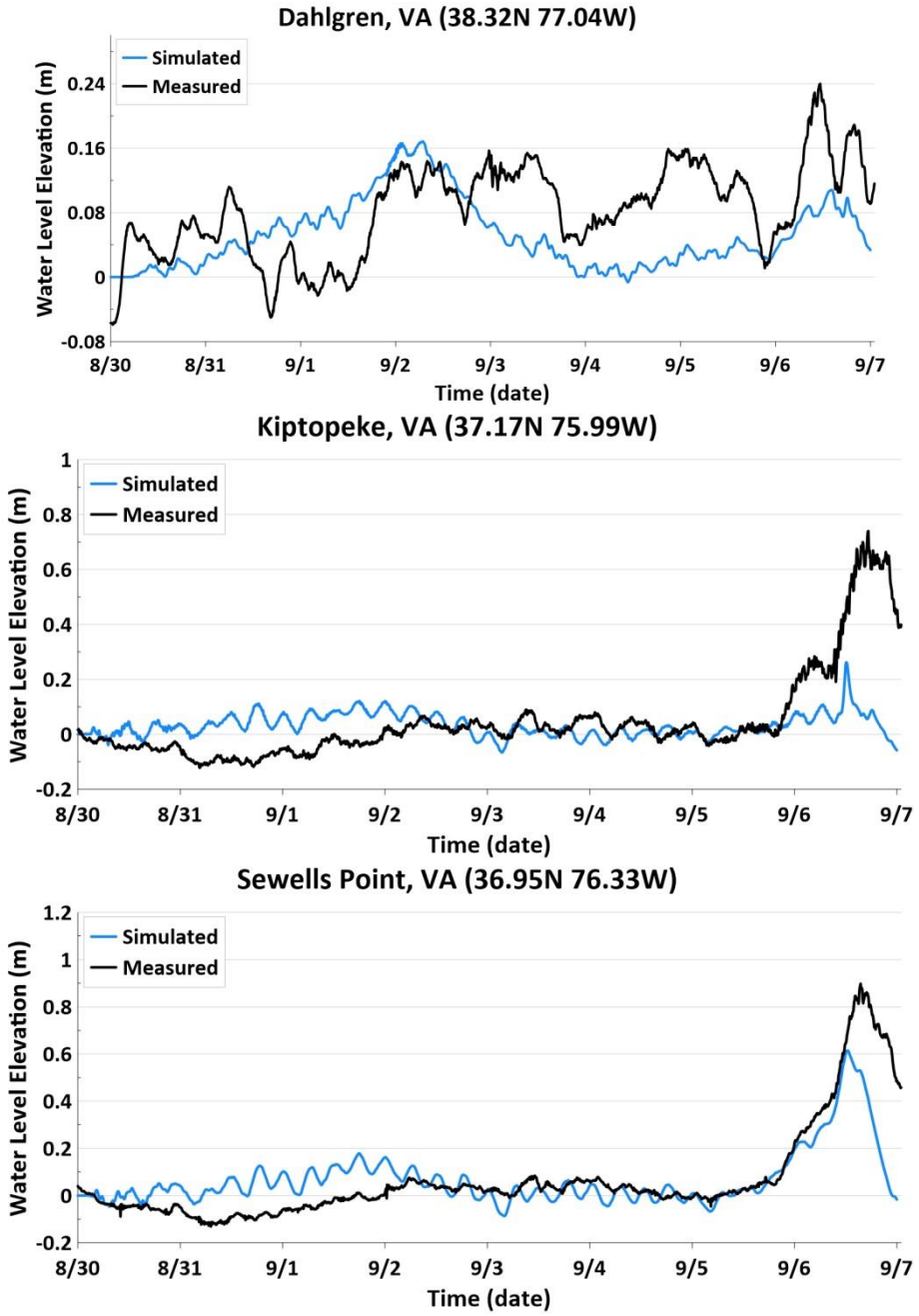

The mean sea level of NOS tide gauges is determined with respect to National Tidal Datum Epoch defined by NOAA. On the other hand, the bathymetry used in the NAMI DANCE simulation is in the WGS84 coordinate system. In the report of Edwing, 2010

(https://www.iwr.usace.army.mil/portals/70/docs/projects/02feb10/2_2_10_trilateral_edwing.pdf) the vertical datum difference in Virginia, U.S. is stated as ~0.16 m. Therefore; 0.16m value is taken out from the stations' data and then compared with computed values.

The computed water level time history is in fairly well aggrement with the recorded stations' time series except from Dahlgren gauge point. On the other hand, it can be seen that NAMI DANCE does not reach the peak values regarding water level when compared with the gauge stations' data. Because NAMI DANCE computes only long-period waves and do not include the wind and wave set-up and the resultant surge due to short-period waves.

In addition, the results of simulations with Nested-1 domain, where -the Bahamas, the most damaged region is located- are shown in Figure 5.12 and Figure 5.13. In the report of NHC (AL052019, 2020), it is stated that ~1.95 m (6.4ft) water level is observed at Grand Bahama island; however, there is not station data in this location.

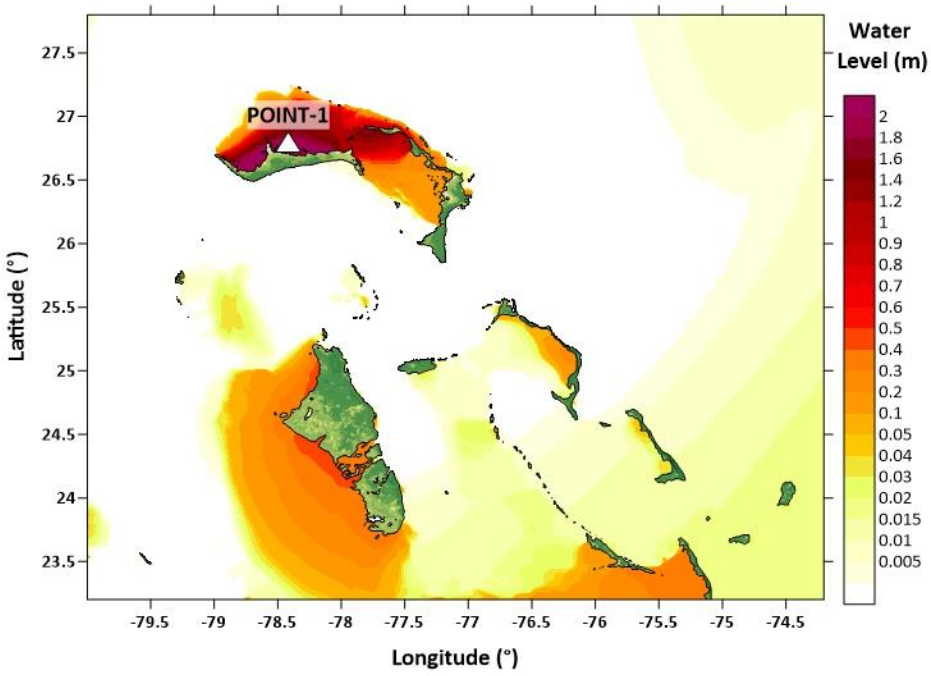

Figure 5.12 The maximum water level distribution of the nested 1 domain

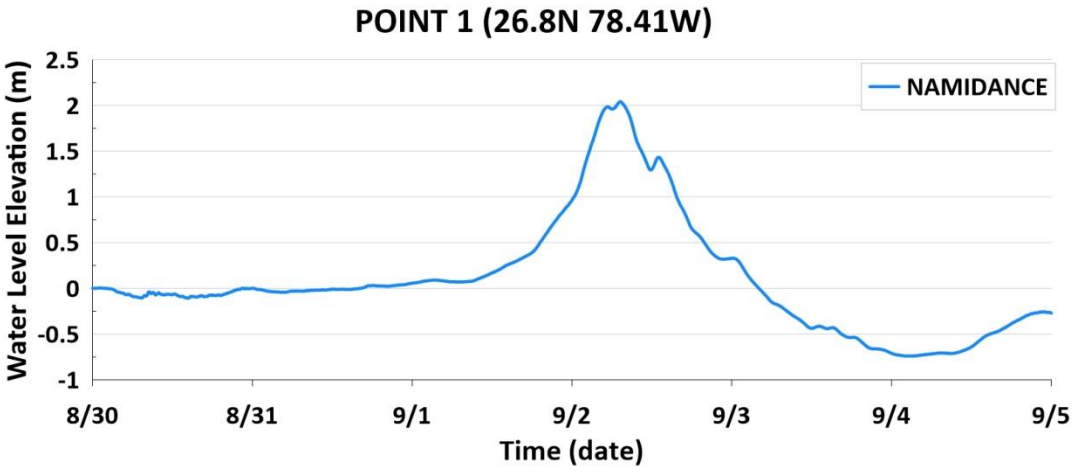

Figure 5.13 The time history of water level at the selected gauge point near Grand Bahama Island where maximum observation is observed as 1.95 m

It is seen from the Figure that the simulated maximum water level meets with the observation as ~1.95 m at Grand Bahamas coast.

CHAPTER 6

SUMMARY AND CONCLUSION

The vast majority of the world's population lives along the coasts, rich in natural resources and ecosystems and give economic opportunities for societies. On the other hand, Coastal areas are threatened by different natural hazards that result in losses of lives and properties. In the assessment of natrural hazards, the numerical modeling is one of the effective tools. However, valid and verified models are the main requirement for the accurate analysis of the hazards. Therefore, validation and verification of the numerical models need to be applied to the internationally accepted benchmark problems.

NAMI DANCE and DELFT3D numerical models are applied to the selected Benchmark Problems of NTHMP tsunami current workshop (http://coastal.usc.edu/currents_workshop/index.html). The selected Benchmark Problems are March 11, 2011, Japan Tsunami waves at Hilo Harbor, Hawaii (Benchmark Problem 2) and the Seaside Oregon State University Model Lab (Benchmark Problem 4). The simulation results of both models are compared with each other and the data of the Benchmark Problems. The FLOW3D results (Sogut, Yalciner, Zaytsev, 2016) are also used in the comparisons in the Benchmark Problem 4.

In Benchmark Problem 2, the arrival times of the computed velocity components are found to agree with the arrival time in the recorded data. On the other hand, DELFT3D, overpredics the S-N component of the velocity at specific intervals. Due to the tsunami currents' sampling rate, some peak values may be missing from the recorded data. In terms of the velocity time series, both models follow a similar pattern with each other. Even if the measured data is resampled, the flow content may not be determined correctly due to the significantly low sampling interval (6

min) of the measured data. At Hilo Tide Station, the water levels are measured. The measured and computed time histories of water level elevation at Hilo Tide Station are compared. The arrival times of both models are found to have a very short time lag. However, the wave patterns coincide with the measurement at t=9 hours.

In Benchmark Problem 4, the computed time series of overland flow depth, cross-shore velocity, and cross-shore momentum flux at the locations B1, B4, B6, and B9 are compared with the experimental data. It is observed that the computed time histories of these parameters by NAMI DANCE, DELFT3D and FLOW3D are in agreement. At location B1, NAMIDANCE results indicate that the wave arrives sooner (by less than a second), whereas FLOW3D underpredicts the flow depth. On the other hand, the DELFT3D results indicate that the time history of overland flow depth corresponds to the measured data in terms of arrival time, and the trend exhibits more coherence than the other two models. At location B4, immediately after the initial peak of the flow depth, all three methods and the measurements agree on the fit. At location B6, the NAMIDANCE results agreed with the experimental results in terms of arrival time. However, the DELFT3D result is delayed in reaching B6. The wave does not reach location B9 in DELFT3D's 40-second simulation period. It is worth noting that FLOW3D produced comparable results at B9. As indicated, as the wave propagates towards the macro roughness region, the flow depth decreases. For all four locations, DELFT3D underestimates the cross-shore velocity. NAMI DANCE simulation results regarding to cross-shore velocity show the same trend as the measured data at B1 and B4 locations if the arrival time coincide with measured since there is very short time lag between them. Except for the arrival times at B1 and B4, the time history of the NAMI DANCE cross-shore momentum flux is consistent with the experimental results at B1, B4, and B6. Additionally, the FLOW3D result at locations B1 and B4 is underestimated compared to the experiment and the other two models concerning the cross-shore momentum flux. Also, DELFT3D underestimates the cross-shore momentum flux at B1 and B4. The maximum values of overland flow depth, cross-

shore velocity and cross-shore momentum flux of the three models and the experiment results are in in Table 6.1.

Table 6.1 The maximum values in BMP 4

		Experiment	NAMI DANCE	DELFT3D	FLOW3D
Overland Flow Depth (m)	**B1**	0.22	0.17	0.16	0.14
	B4	0.16	0.12	0.11	0.12
	B6	0.091	0.056	0.066	0.087
	B9	0.0444	0.0166	0	0.0242
Cross-Shore Velocity (m/s)	**B1**	2.04	2.16	1.5	1.54
	B4	1.79	1.6	1.52	1.92
	B6	1.96	1.55	0.98	1.91
	B9	1.4	0.55	0	0.73
Cross-Shore Momentum Flux (m^3/s^2)	**B1**	0.96	0.8	1.09	0.27
	B4	0.57	0.53	0.72	0.36
	B6	0.21	0.35	0.36	0.3
	B9	0.034	0.0114	0	0.0091

The tropical cyclone Dorian, which hit the western Atlantic and Caribbean in September 2019, is simulated by NAMI DANCE using its new module for tropical cyclone events. The simulation is performed using the HRES meteorological data (spatial and temporal change of pressure and wind field) as input from August 30 to September 7, 2019. The recorded data at tide stations and the computed time-series of water level are compared. Except for the Dahlgren gage point, the computed time histories of water level agreed reasonably well with the recorded time series of water level at the stations. On the other hand, when comparing the recorded data at the tide stations, it can be observed that NAMI DANCE does not reach the peak levels of water. Because NAMI DANCE only calculates long waves and do not incorporate short-term waves, wind and wave set-up and the resulting surge. Furthermore, it is shown that the calculated result of Nested-1 domain and data from the simulated maximum water level at Grand Bahamas coast, which is

the most damaged area indicated by the National Hurricane Center, matches the observation at approx. 1.95 meters above sea level.

The experience and the results of the study indicate that NAMI DANCE and DELFT3D compute the results of Benchmark Problems 2 and 4 in agreement with the measurements. Furthermore NAMI DANCE sucessfully simulated tropical cyclone Dorian and close agrement between the computed results and measurements/observations are obtained. It is recommended higher spatial and temporal resolution of atmospheric pressure and wind fields lead to more accurate results by NAMI DANCE.

REFERENCES

Arcos, M. E. M., & LeVeque, R. J. (2015). Validating velocities in the GeoClaw tsunami model using observations near Hawaii from the 2011 Tohoku tsunami. Pure and Applied Geophysics, 172(3-4), 849-867.

Aristizabal-Vargas, M. F., Miles, T., Glenn, S., Kim, H. S., & Mehra, A. (2020, October). Validation of the HWRF-POM and HWRF-HYCOM hurricane forecasting systems during Hurricane Dorian using glider observations. In Global Oceans 2020: Singapore–US Gulf Coast (pp. 1-5). IEEE.

Berger, M. J., & Leveque, R. J. (1998). Adaptive mesh refinement using wave-propagation algorithms for hyperbolic systems. SIAM Journal on Numerical Analysis, 35(6), 2298-2316.

Blumberg, A. F., & Mellor, G. L. (1987). A description of a three-dimensional coastal ocean circulation model. Three-dimensional coastal ocean models, 4, 1-16.

Chau, K. W. (2010). Modelling for coastal hydraulics and engineering. CRC Press.Goto, C., Ogawa, Y., Shuto, N., & Imamura, F. (1997). Numerical method of tsunami simulation with the leap-frog scheme. IOC Manuals and Guides, 35, 130.

Choi, Y. K., & Jo, T. C. (2018). Dynamics of surface and internal long waves generated by atmospheric pressure disturbances. Applied Ocean Research, 76, 61-70.

Cox, D., T. Tomita, P. Lynett, and R.A. Holman. (2008). Tsunami Inundation with Macroroughness in the Constructed Environment. Proceedings of 31st International Conference on Coastal Engineering, ASCE, (pp. 1421–1432).

Deltares, D. (2013). Delft3D-FLOW user manual.

DOGAMI (Oregon Department of Geology and Mineral Industries), 2001. “Senate Bill379.” Portland, OR. Retrieved from: Oregon Geospatial Enterprise Office (GEO) http://cms.oregon.gov/DAS/CIO/GEO/Pages/index.aspx.

Dogan, G. G., Pelinovsky, E., Zaytsev, A., Metin, A. D., Tarakcioglu, G. O., Yalciner, A. C., Yalciner, B. & Didenkulova, I. (2021). Long wave generation and coastal amplification due to propagating atmospheric pressure disturbances. Natural Hazards, 106(2), 1195-1221.

Duputel, Z., Rivera, L., Kanamori, H., & Hayes, G. (2012). W phase source inversion for moderate to large earthquakes (1990–2010). Geophysical Journal International, 189(2), 1125-1147.

Horrillo, J., Grilli, S. T., Nicolsky, D., Roeber, V., & Zhang, J. (2015). Performance benchmarking tsunami models for NTHMP’s inundation mapping activities. Pure and Applied Geophysics, 172(3), 869-884.

Horsburgh, K., & De Vries, H. (2011). Guide to storm surge forecasting. World Meteorological Organisation.

Hurricane FAQ. NOAAs Atlantic Oceanographic and Meteorological Laboratory. (2021, June 1). https://www.aoml.noaa.gov/hrd-faq/.

Imamura, F. (1989). Tsunami Numerical Simulation with the staggered leap-frog scheme (Numerical code of TUNAMI-N1), School of Civil Engineering, Asian Inst. Tech. and Disaster Control Research Center, Tohoku University

Imamura, F. (1996). Review of tsunami simulation with a finite difference method. Long-wave runup models, 25-42.

Imamura, F., Yalciner, A. C., & Ozyurt, G. (2006). Tsunami modelling manual. UNESCO IOC international training course on Tsunami Numerical Modelling.

Jelenak, Z., Sapp, J., Alsweiss, S., & Chang, P. S. (2020). AMSR-2 OBSERVATIONS OF HURRICANE DORIAN. In IGARSS 2020-2020 IEEE International Geoscience and Remote Sensing Symposium (pp. 5982-5985). IEEE.

Johnson, H. (n.d.). Hilo Bay [Photograph]. University of Hawaii, Hilo, Hawaii, USA.

Lekkas, E. L., Andreadakis, E., Kostaki, I., & Kapourani, E. (2013). A proposal for a new integrated tsunami intensity scale (ITIS-2012). Bulletin of the Seismological Society of America, 103(2B), 1493-1502.

Lynett, P., Borrero, J., Son, S., Wilson, R., and Miller, K. (2014). Assessment of Current-Induced Tsunami Hazards for Maritime Planning. Geophys. Res. Letts., 41.

Lynett, P. J., Gately K., Wilson R., Montoya L., Arcas D., Aytore B., Bai Y., Bricker J. D., Castro M. J., Cheung, K. F. David G. C., Dogan G. G., Escalante C., González-Vida J. M., Grilli S. T., Heitmann T. W., Horrillo J., Kânoglu U., Kian R., Kirby J. T., Li W., Macías J., Nicolsky D. J., Ortega S., Pampell-Manis A., Park Y. S., Roeber V., Sharghivand N., Shelby M., Shi F., Tehranirad B., Tolkova E., Thio H. K., Velioglu D., Yalciner A. C., Yamazaki Y., Zaytsev, A., Zhang Y. J., (2017), "Inter-model analysis of tsunami-induced coastal currents", Ocean Modelling, 114 (2017) 14–32, http://dx.doi.org/10.1016/j.ocemod.2017.04.003

Maguire, A. E. (2011). Hydrodynamics Control and Numerical Modelling of Absorbing Wavemakers. Ph.D. Thesis. The University of Edinburgh.

Mattocks, C., & Forbes, C. (2008). A real-time, event-triggered storm surge forecasting system for the state of North Carolina. Ocean Modelling, 25(3-4), 95-119.

Mohanty, U. C., & Gopalakrishnan, S. G. (Eds.). (2016). Advanced numerical modeling and data assimilation techniques for tropical cyclone predictions. Springer.

Mori, N., Takahashi, T., Yasuda, T., & Yanagisawa, H. (2011). Survey of 2011 Tohoku earthquake tsunami inundation and run-up. Geophysical research letters, 38(7).

NATIONAL HURRICANE CENTER. (2020, April). Tropical Cyclone Report Hurricane Dorian ((AL052019)). https://www.nhc.noaa.gov/data/tcr/AL052019_Dorian.pdf

National Tsunami Hazard Mitigation Program. (2015). NTHMP Subcommittees & Annual Meeting. Portland, Oregon.

NOAA, 2011. West Coast/Alaska Tsunami Warning Center, NOAA/NWS TSUNAMI of 11 March, 2011 (Honshu, Japan) [online]. Available at: <http://wcatwc.arh.noaa.gov/previous.events/03-11-11_Honshu/03-11-11.htm>.

Park, H., Cox, D. T., Lynett, P. J., Wiebe, D. M. and Shin, S. (2013). Tsunami Inundation Modeling in Constructed Environments: A Physical and Numerical Comparison of Free-Surface Elevation, Velocity, and Momentum Flux. Coastal Engineering, 79, 9–21.

Rueben, M., R. Holman, D. Cox, S. Shin, J. Killian, and J. Stanley. (2011). Optical Measurements of Tsunami Inundation Through an Urban Waterfront Modeled in a Large-Scale Laboratory Basin. Coastal Engineering, 58, 229 – 238.

Sanders, Kerry; Silva, Daniella (22 December 2019). "Months after Hurricane Dorian, Abaco Islands still completely devastated". NBC News. Retrieved 23 April 2020.

Shi, F., Kirby, J. T., & Tehranirad, B. (2012). Tsunami benchmark results for spherical coordinate version of FUNWAVE-TVD. Center for Applied Coastal Research, University of Delaware, Tech. Rep, CACR-12-02.

Shuto, N., Goto, C., & Imamura, F. (1990). Numerical simulation as a means of warning for near field tsunamis. Coastal Engineering in Japan. 33, No: 2, 173–193

Sozdinler, C. O., Yalciner, A. C., Zaytsev, A., Suppasri, A., & Imamura, F. (2015). Investigation of hydrodynamic parameters and the effects of breakwaters during the 2011 Great East Japan Tsunami in Kamaishi Bay. Pure and Applied Geophysics, 2015 Springer Basel DOI 10.1007/s00024-015-1051-8

Synolakis, C. E., Bernard, E. N., Titov, V. V., Kanoglu, U. and Gonzalez, F. (2007). Standards, Criteria, and Procedures for NOAA Evaluation of Tsunami Numerical Models.55 p. Seattle, Washington: NOAA OAR Special Report, Contribution No 3053, NOAA/OAR/PMEL.

Titov, V. V., & Synolakis, C. E. (1995). Modeling of breaking and nonbreaking long-wave evolution and runup using VTCS-2. Journal of Waterway, Port, Coastal, and Ocean Engineering, 121(6), 308-316.

U.S. Geological Survey. (n.d.). 20 Largest Earthquakes in the World. Retrieved January 20, 2021, from https://www.usgs.gov/natural-hazards/earthquake-hazards/science/20-largest-earthquakes-world?qt-science_center_objects=0#qt-science_center_objects

Velioğlu, D., Cevdet Yalçıner, A., & Zaytsev, A. (2016, April). Validation and Comparison of 2D and 3D Codes for Nearshore Motion of Long Waves Using Benchmark Problems. In EGU General Assembly Conference Abstracts (pp. EPSC2016-2925).

Velioğlu, D. (2017). Advanced two-and three-dimensional Tsunami models: benchmarking and validation.

Yablonsky, R. M., Ginis, I., & Thomas, B. (2015). Ocean modeling with flexible initialization for improved coupled tropical cyclone-ocean model prediction. Environmental Modelling & Software, 67, 26-30.

Yalciner, A. C., Suppasri, A., Mas, E., Kalligeris, N., Necmioglu, O., Imamura, F., ... & Synolakis, C. (2011). Field survey on the coastal impacts of March 11, 2011 Great East Japan tsunami. Proceedings of Seismic Protection of Cultural Heritage.

Yalciner, Ahmet & Zaytsev, Andrey & Kânoğlu, Utku & Gozde, Guney & Velioglu Sogut, Deniz & Kian, Rozita & Aytore, Betul & Sharghivand, Naeimeh. (2015). NAMI DANCE Benchmark Results.

Zhang, Y., Jiang, Z., Fang, Y., & Cheng, X. (2014, March). Analysis and interpretation of tsunami damage caused by the 2011 Japan earthquake using ENVISAT ASAR images. In Proceeding of the 35th International Symposium on Remote Sensing of Environment.

APPENDICES

A. Meteorological Input for Tropical Cyclone Dorian Case Study

The mean sea level pressure taken from the ECMWF HRES dataset is shown below in Figure A.1 with the 12 hours time interval for the coarse domain.

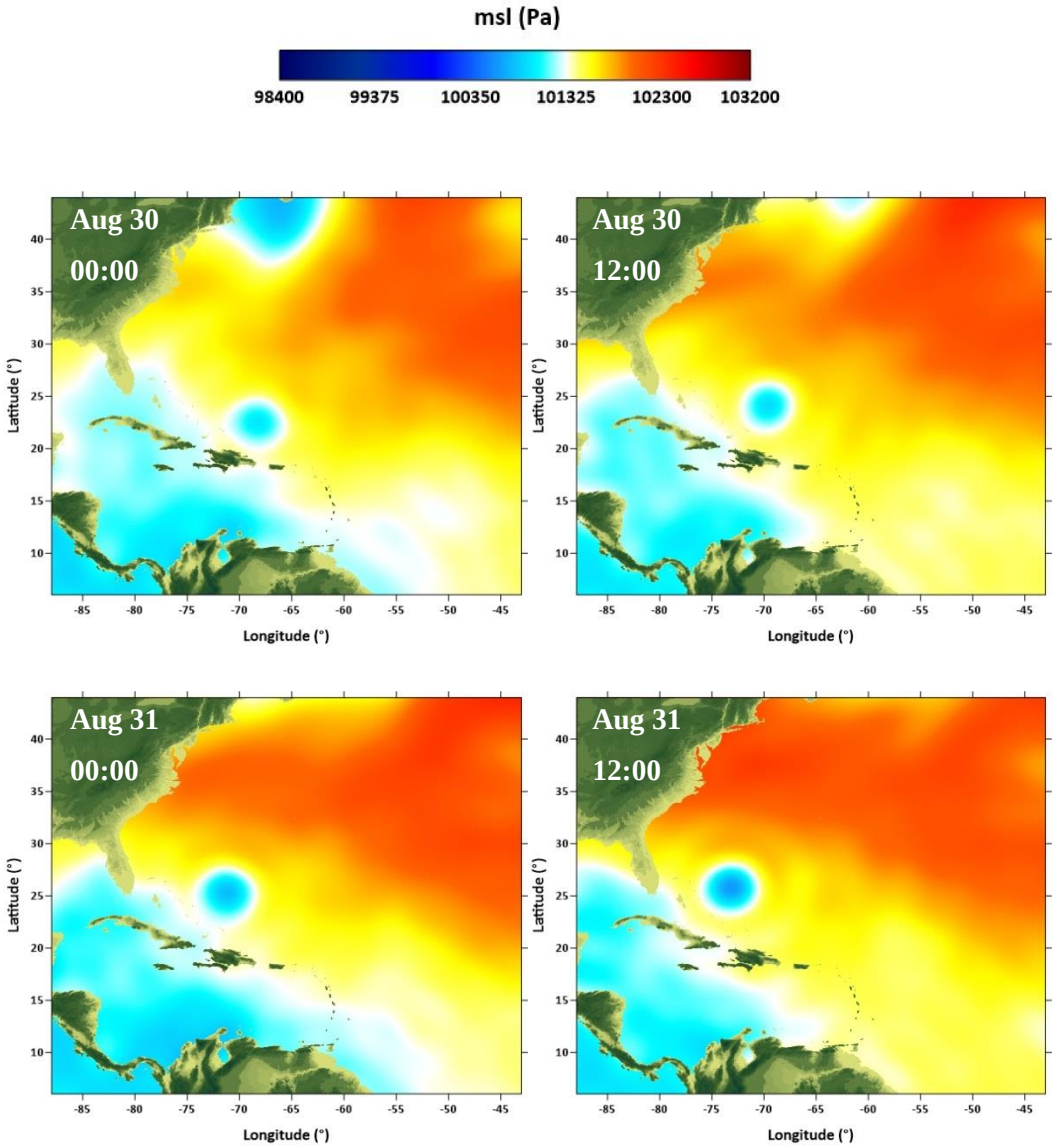

Figure A.1 (continued)

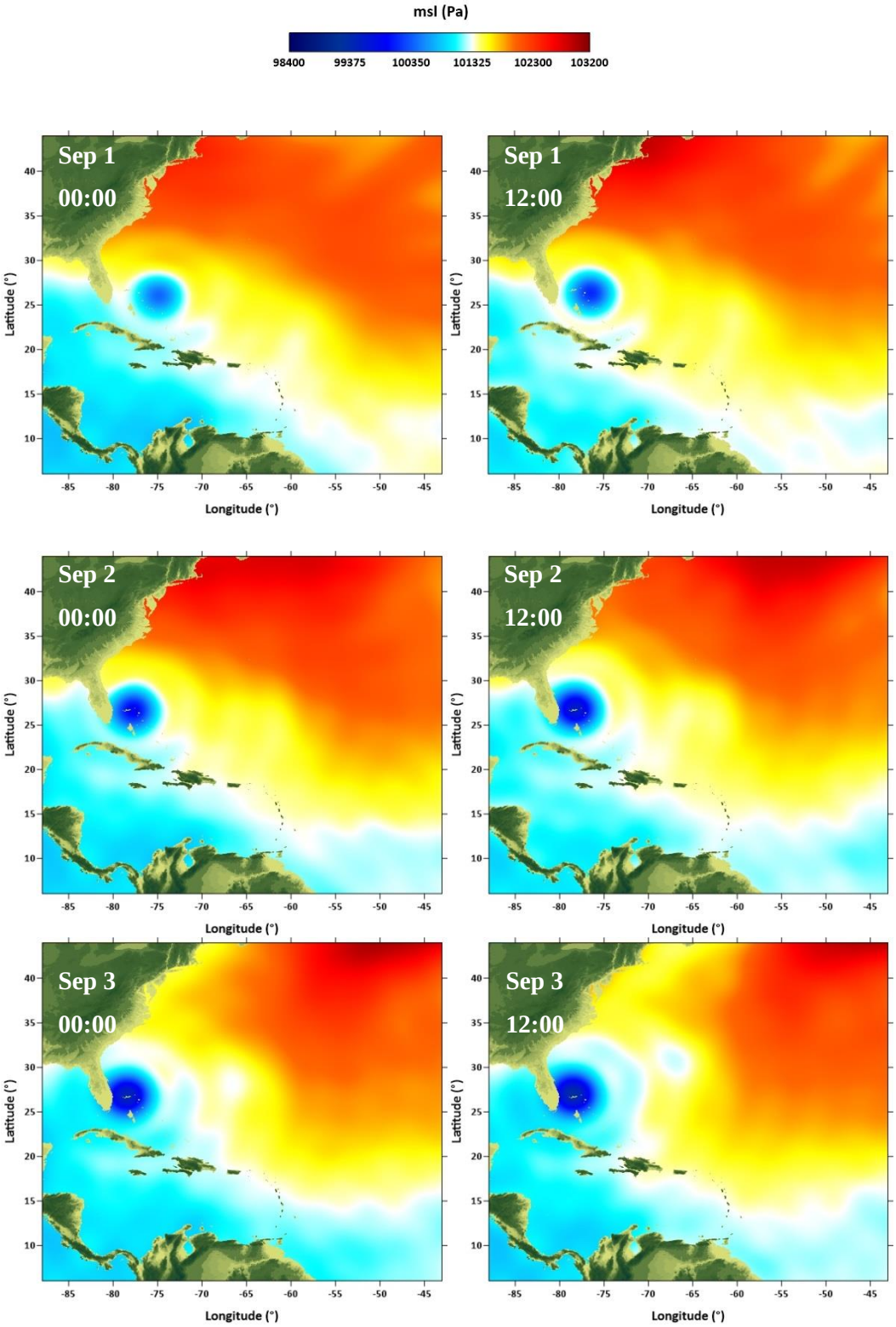

Figure A.1 (continued)

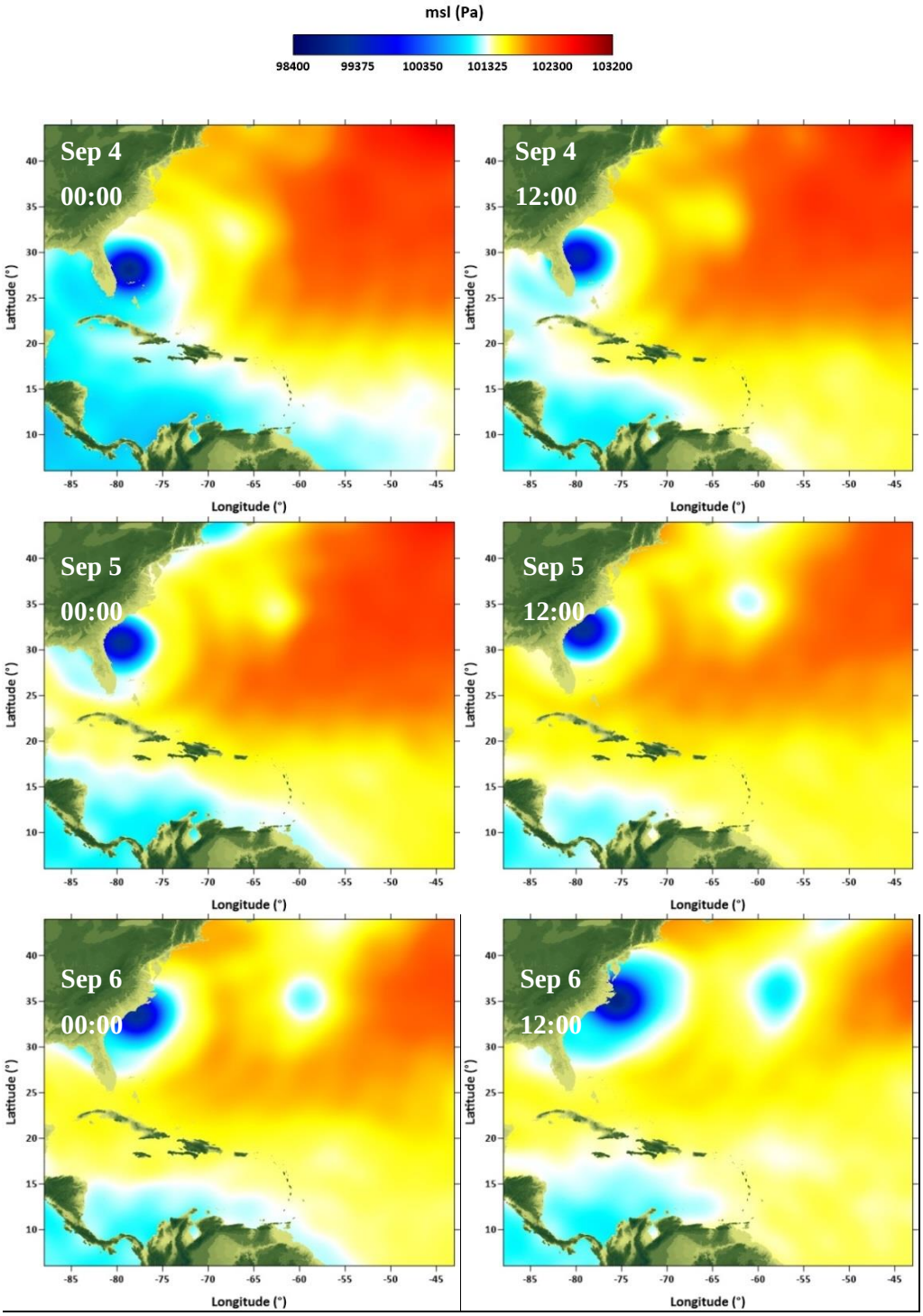

Figure A.1 Mean Sea Level Pressure input for Tropical Cyclone Dorian simulations

The east-west component (u component) of wind taken from the ECMWF HRES dataset is shown below in Figure A.2 with the 12 hours time interval for the coarse domain.

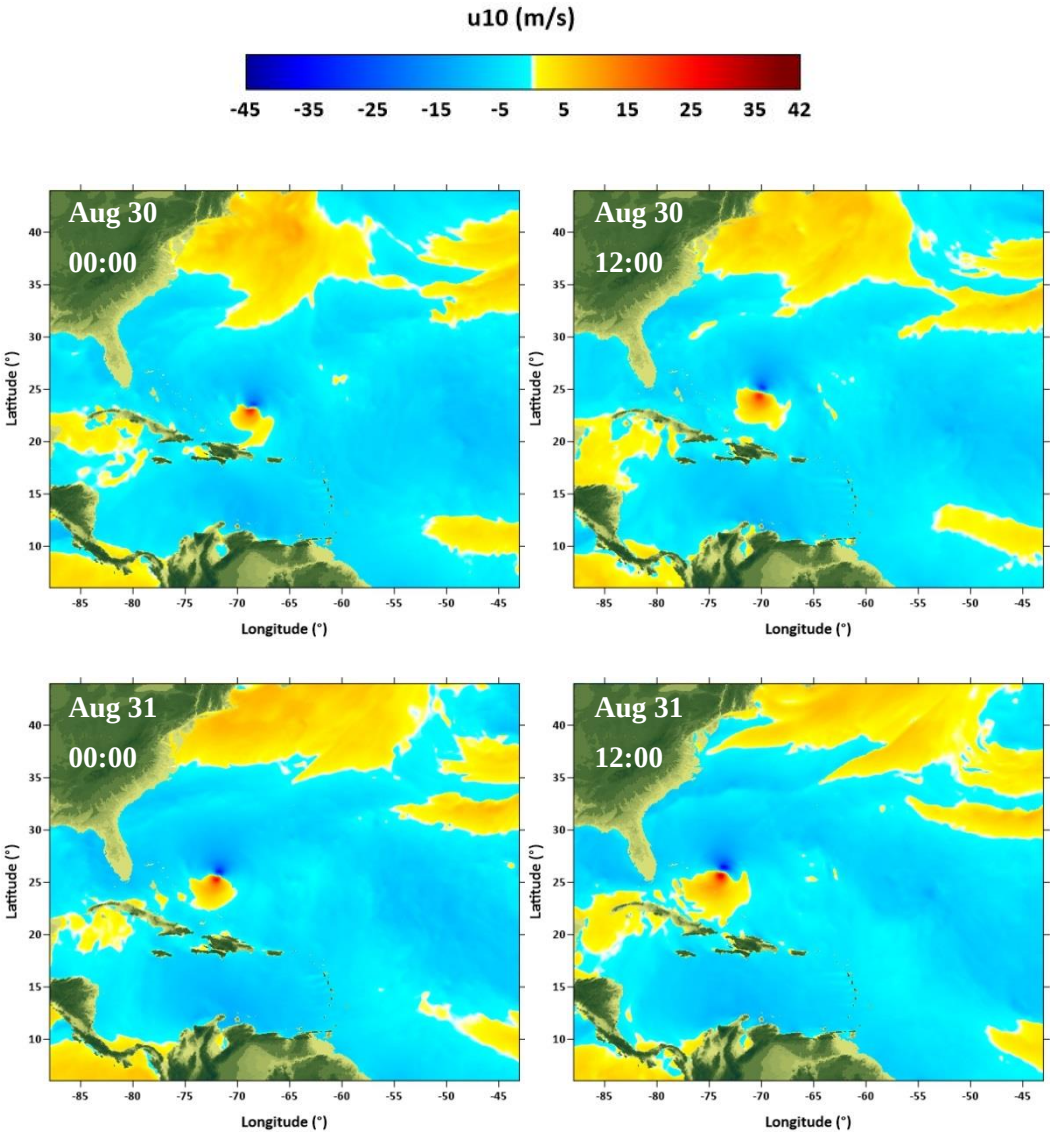

Figure A.2 (continued)

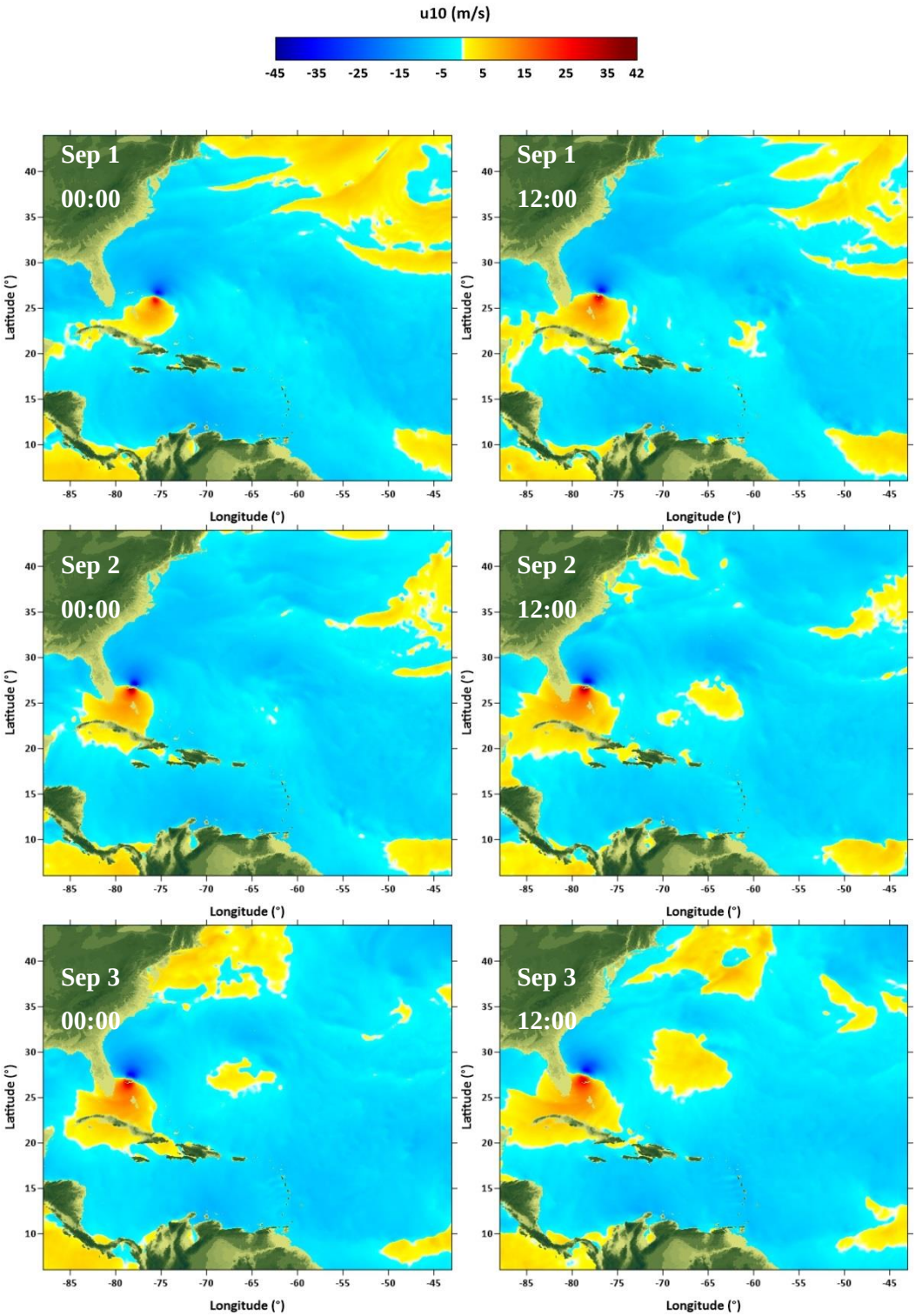

Figure A.2 (continued)

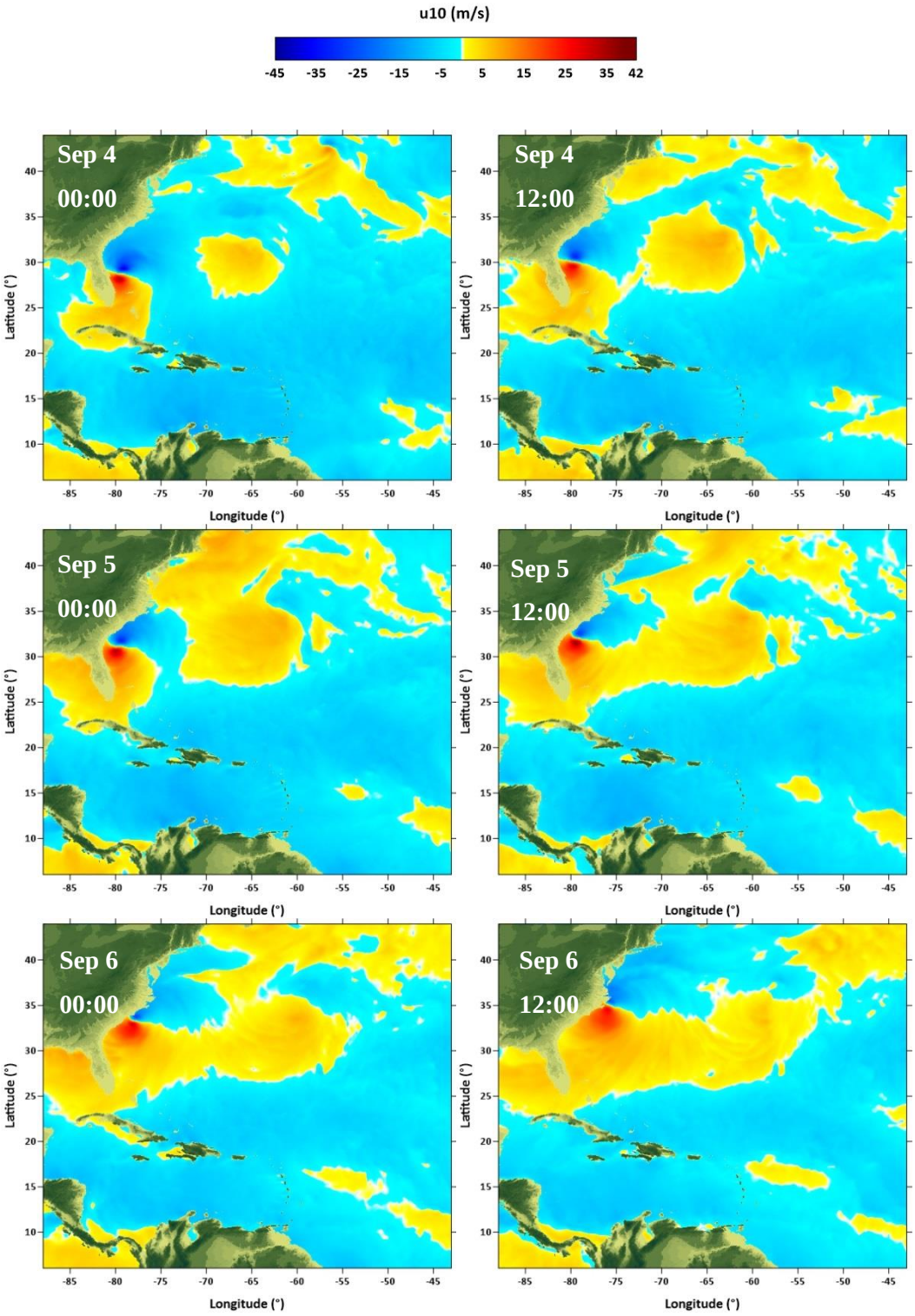

Figure A. 2 U-component of wind input for Tropical Cyclone Dorian simulations

The north-south component (v component) of wind taken from the ECMWF HRES dataset is shown below in Figure A.3 with the 12 hours time interval for the coarse domain.

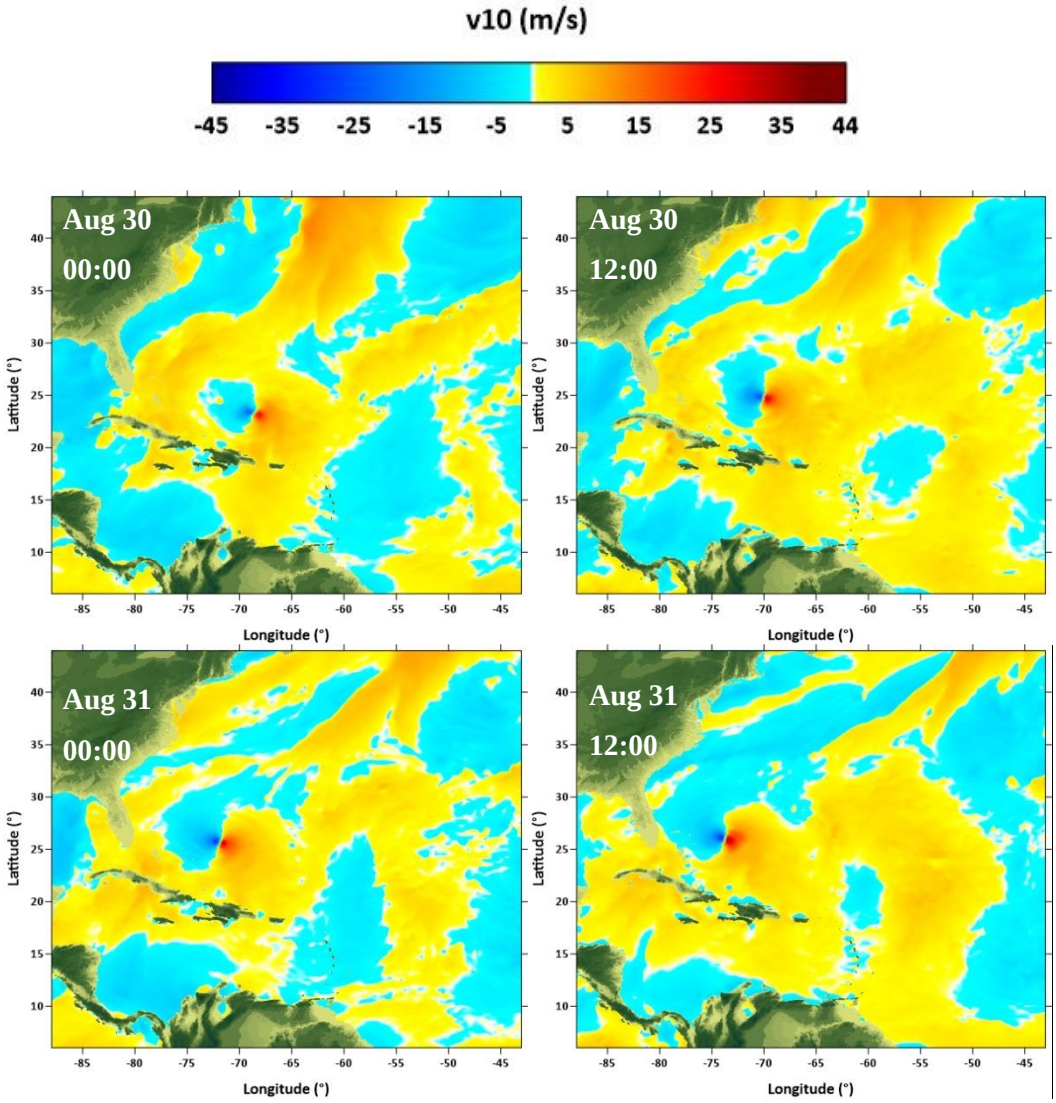

Figure A.3 (continued)

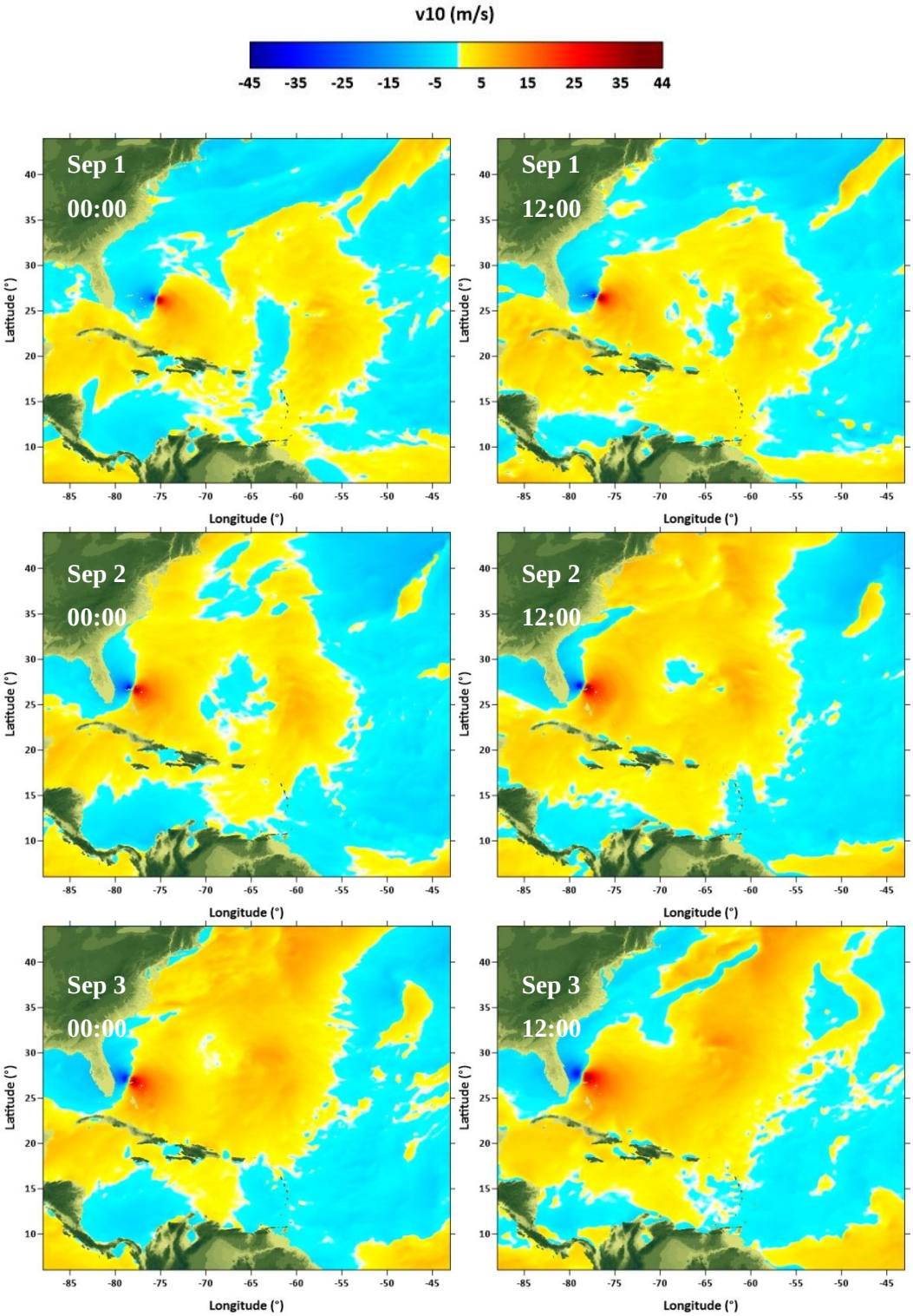

Figure A.3 (continued)

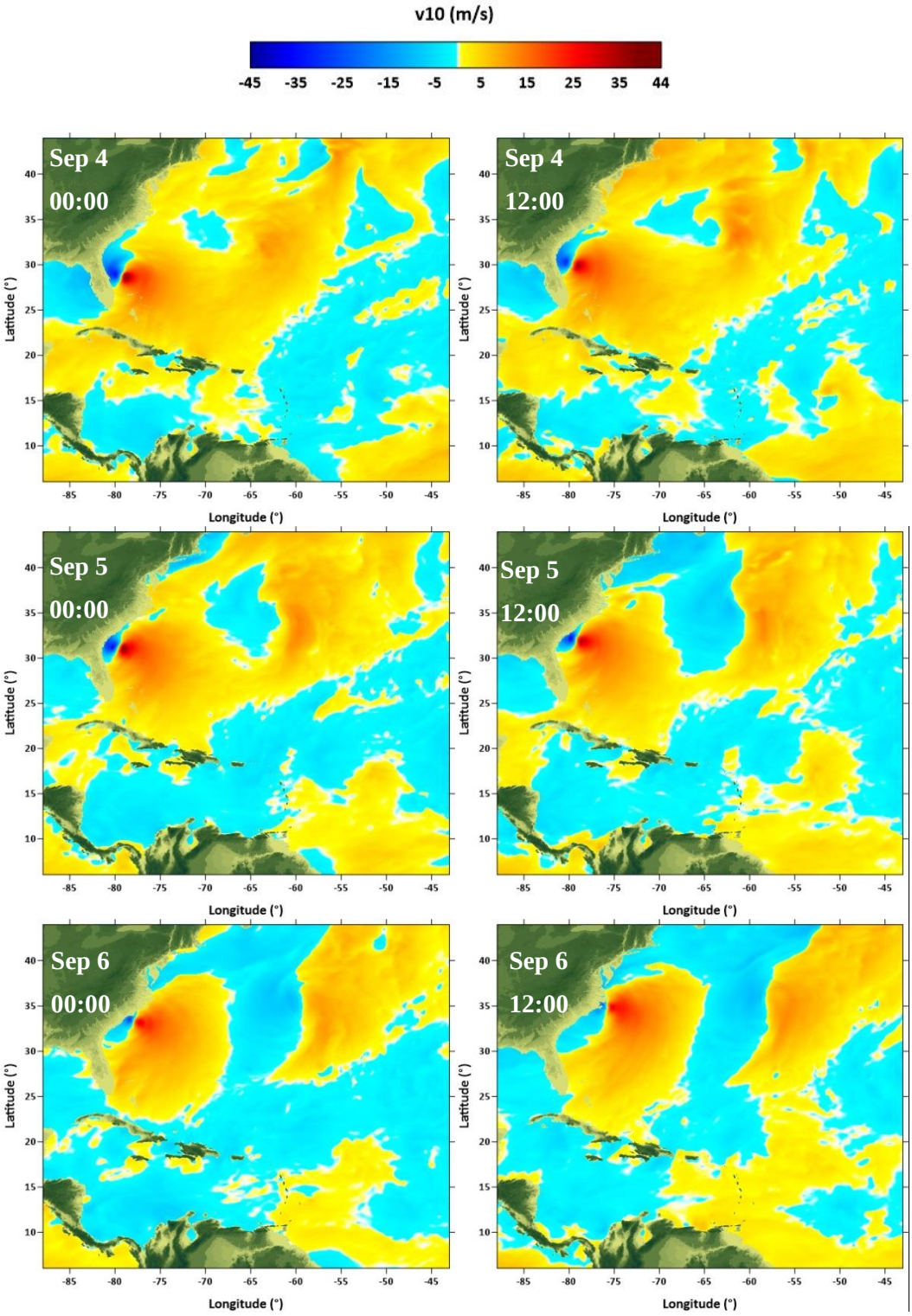

Figure A. 3 V-component of wind input for Tropical Cyclone Dorian simulations